Article

Cell

Intermittent Pili-Mediated Forces Fluidize *Neisseria meningitidis* Aggregates Promoting Vascular Colonization

Graphical Abstract

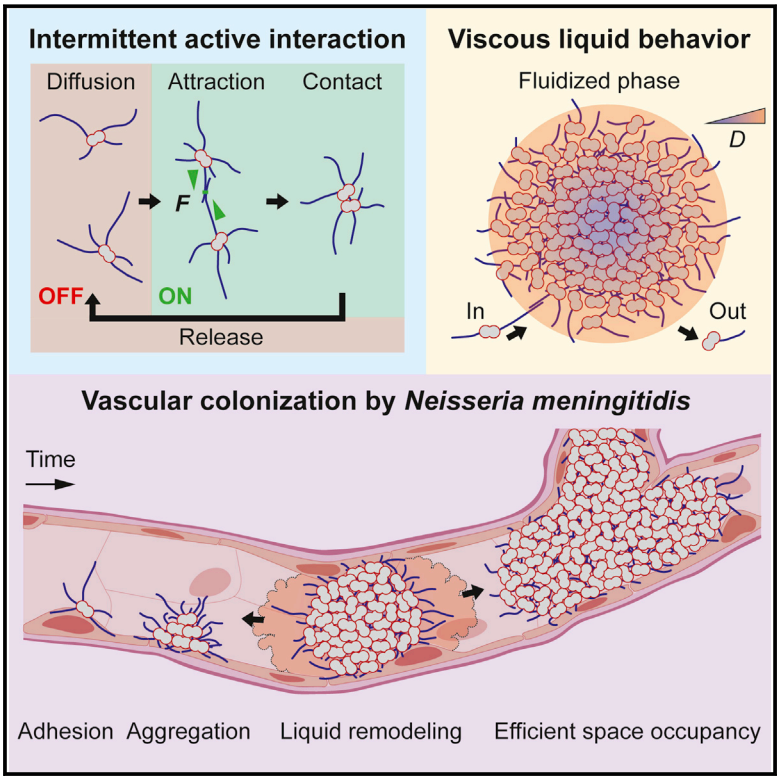

Highlights

- Aggregates of meningococci behave as a viscous liquid with a unique fluidized phase
- This behavior depends on type IV pili-mediated intermittent bacterial attractions
- Based on such intermittence, a phase diagram of aggregation phenotypes can be defined
- Liquid-like aggregates adapt to the geometry of capillaries for efficient colonization

Authors

Daria Bonazzi, Valentina Lo Schiavo, Silke Machata, ..., Hugues Chaté, Raphael Voituriez, Guillaume Duménil

Correspondence

guillaume.dumenil@pasteur.fr

In Brief

Meningitis-causing bacteria form viscous fluid aggregates in blood vessels with high bacterial diffusion that enhance infection.

Bonazzi et al., 2018, Cell *174*, 1–13
June 28, 2018
https://doi.org/10.1016/j.cell.2018.04.010

CellPress

Please cite this article in press as: Bonazzi et al., Intermittent Pili-Mediated Forces Fluidize *Neisseria meningitidis* Aggregates Promoting Vascular Colonization, Cell (2018), https://doi.org/10.1016/j.cell.2018.04.010

Intermittent Pili-Mediated Forces Fluidize *Neisseria meningitidis* Aggregates Promoting Vascular Colonization

Daria Bonazzi,[1,8] Valentina Lo Schiavo,[1,8] Silke Machata,[1] Ilyas Djafer-Cherif,[2] Pierre Nivoit,[1] Valeria Manriquez,[1] Hirokazu Tanimoto,[3] Julien Husson,[4] Nelly Henry,[5] Hugues Chaté,[2,6,7] Raphael Voituriez,[5,7] and Guillaume Duménil[1,9,*]

[1]Pathogenesis of Vascular Infections Unit, INSERM, Institut Pasteur, 75015 Paris, France
[2]Service de Physique de l'Etat Condensé, CEA, CNRS, Université Paris-Saclay, 91191 Gif-sur-Yvette, France
[3]Institut Jacques Monod, 75013 Paris, France
[4]Laboratoire d'Hydrodynamique (LadHyX), Department of Mechanics, Ecole Polytechnique-CNRS UMR7646, 91128 Palaiseau, France
[5]Laboratoire Jean Perrin, CNRS UMR 3231, Université Pierre et Marie Curie, 75005 Paris, France
[6]Computational Science Research Center, Beijing 100193, China
[7]Laboratoire de Physique Théorique de la Matière Condensée, CNRS, Université Pierre et Marie Curie, 75005 Paris, France
[8]These authors contributed equally
[9]Lead Contact
*Correspondence: guillaume.dumenil@pasteur.fr
https://doi.org/10.1016/j.cell.2018.04.010

SUMMARY

Neisseria meningitidis, a bacterium responsible for meningitis and septicemia, proliferates and eventually fills the lumen of blood capillaries with multicellular aggregates. The impact of this aggregation process and its specific properties are unknown. We first show that aggregative properties are necessary for efficient infection and study their underlying physical mechanisms. Micropipette aspiration and single-cell tracking unravel unique features of an atypical fluidized phase, with single-cell diffusion exceeding that of isolated cells. A quantitative description of the bacterial pair interactions combined with active matter physics-based modeling show that this behavior relies on type IV pili active dynamics that mediate alternating phases of bacteria fast mutual approach, contact, and release. These peculiar fluid properties proved necessary to adjust to the geometry of capillaries upon bacterial proliferation. Intermittent attractive forces thus generate a fluidized phase that allows for efficient colonization of the blood capillary network during infection.

INTRODUCTION

Mechanisms and principles driving bacterial aggregation are highly diverse, because they depend on the specific properties of the bacterial species involved and the conditions they live in. Bacterial aggregates in the context of biofilms, for instance, are the focus of intense study because of their clinical importance as a mechanism of antibiotic resistance. Their mechanical properties are largely defined by the self-produced matrix comprising DNA, polysaccharides, and proteins, which behave as a hydrated polymeric meshwork. Such structures display viscoelastic properties, combining both viscous fluid and elastic behavior (Persat et al., 2015). A second type of bacterial aggregates relies on bacterial motility. In particular, *Escherichia coli* or *Salmonella typhimurium* are able to form clusters of different shapes and sizes that depend on flagella-based motility and chemotactic cues (Budrene and Berg, 1991).

Another example of motility-driven aggregation is that of *Neisseria gonorrheae*. In this case, the retractile properties of their long filamentous organelles, known as type IV pili (T4P), allow them to move on surfaces, a process known as twitching motility. Combined with interactions between pili this motility promotes bacterial clustering (Taktikos et al., 2015; Oldewurtel et al., 2015). In addition to *Neisseria gonorrhoeae*, T4P are expressed by a large number of Gram-negative bacteria including human pathogens, such as *Vibrio cholerae*, *Pseudomonas aeruginosa*, or *Neisseria meningitidis*, and Gram-positive bacteria, such as *Streptococcus sanguinis*. T4P are several microns long semi-flexible fibers extending out of the bacterial body. In *Neisseria* spp., pili are highly dynamic as they grow and retract at speeds in the order of 1 μm/s. As they retract through an ATP-dependent process, individual pili can generate very high forces, reaching up to 100 pN for single pili and 10-fold this value for bundles of pili (Biais et al., 2008; Maier et al., 2002). Pilus-pilus interaction is thought to promote auto-aggregation.

In *Neisseria meningitidis*, T4P are central virulence factors required for bacterial adhesion along the endothelium and subsequent formation of intravascular aggregates. This vascular colonization process is a prerequisite for vascular damage observed during infection (Melican et al., 2013). *In vitro* studies have shown that aggregates formed by *N. meningitidis* also depend on type IV pili, but the biophysical properties of these clusters and their impact on the infection process have not been characterized. Once bacteria adhere to capillary endothelial cells, they proliferate and progressively occlude the vessel lumen. Growth in the tubular and sometimes tortuous geometry found in capillaries imposes important mechanical constraints that require specific adaptation. This interdisciplinary work

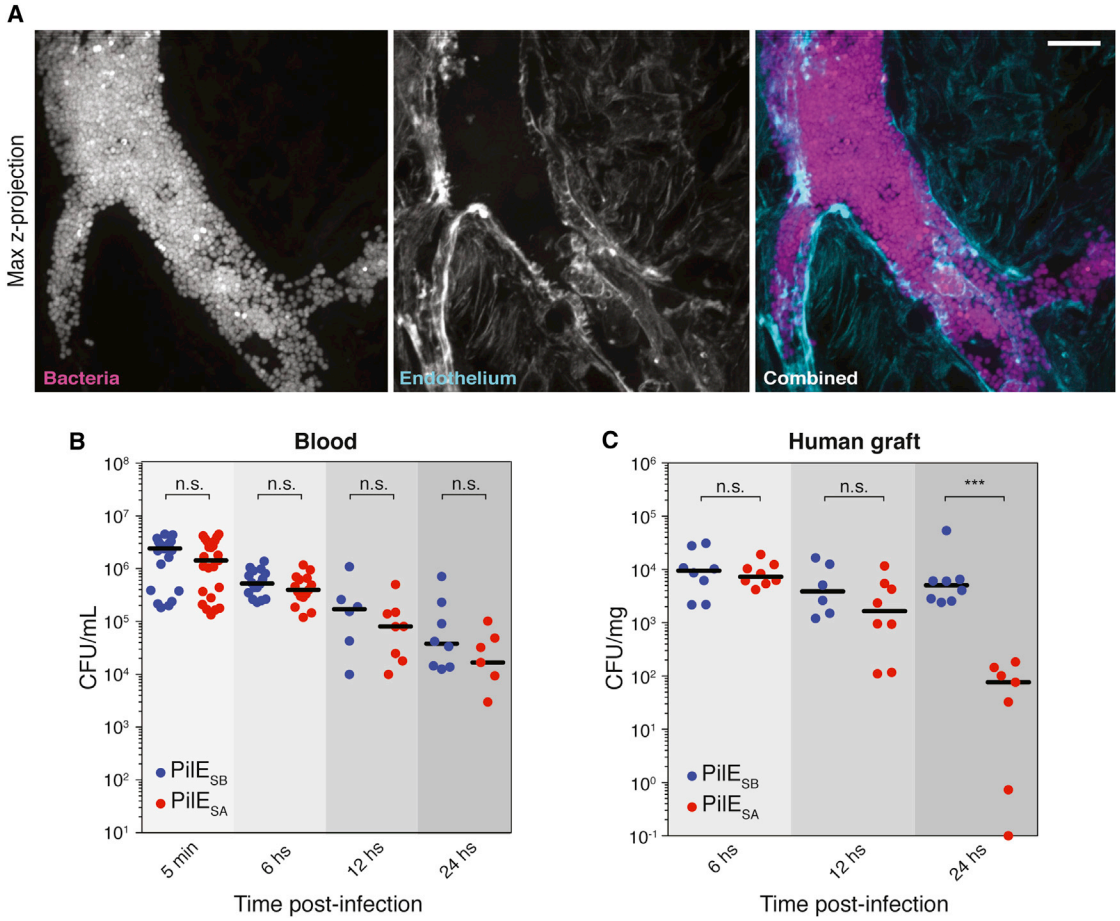

Figure 1. Bacterial Auto-aggregation Enhances Vascular Colonization *In Vivo*

(A) Maximal z-projection from confocal slices of an infected vessel at 6 hr post-infection in a xenograft model of infection showing GFP-expressing *N. meningitidis* aggregates, the human endothelium surface (rhodamin-labeled *Ulex europeus* agglutinin) and corresponding merged image. Scale bar, 10 μm. The image is representative of n = 3 independent experiments, N = 3 mice grafted with human skin from the same donor.

(B) Bacterial colony-forming unit (CFU) counts from the blood of mice grafted with human skin and infected with the *N. meningitidis* pilin variants PilE$_{SB}$ (indicated in blue) and PilE$_{SA}$ (indicated in red). These counts represent the number of bacteria circulating in the blood at a given time point.

(C) Bacterial CFU counts from skin biopsies taken from grafted human skin of mice infected with the *N. meningitidis* pilin variants PilE$_{SB}$ (indicated in blue) and PilE$_{SA}$ (indicated in red). These counts indicated the number of bacteria attached to the capillary endothelium at a given time point. Each data point represents one infected mouse, with corresponding blood and human graft samples. n = 3 independent experiments, N = 6–8 mice. Human skin grafts used for this dataset correspond to 3 donors, and for each experiment mice grafted with human skin from the same donor were infected with the 2 bacterial strains for comparison. Black bars indicate the average values for each condition. ns, not significant; *** p value = 0.0003.

See also Figure S1.

explores how the biophysical properties of *N. meningitidis* aggregates determine human disease progression.

RESULTS

Bacterial Auto-aggregation Enhances Vascular Colonization *In Vivo*

During meningococcal infection, bacterial aggregates can be found in the lumen of capillaries located in most organs, including the brain, but the impact of aggregation on disease progression is unknown (Mairey et al., 2006). Such aggregates also form in human capillaries of a humanized mouse model based on human skin xenograft, which reproduces the key histological features of *N. meningitidis* infection (Melican et al., 2013). In such a model, 6 hr post-infection aggregates filled the vessel lumen along tens to hundreds of micrometers of tortuous and sometimes anastomosed capillary networks (Figure 1A). To assess the role of aggregation, we exploited a naturally occurring variant of the major pilin termed PilE$_{SA}$ (Nassif et al., 1993). This variant occurred spontaneously through a genetic recombination system present in *Neisseria* species (Rotman and Seifert, 2014). In contrast with the frequently occurring PilE$_{SB}$ variant that promotes both adhesion and aggregation, the PilE$_{SA}$ variant selectively promotes adhesion but not aggregation (Figure S1A). At the initial stage of interaction with host cells, individual bacteria from a strain expressing the SA and SB pilin variants had the same ability to adhere to endothelial

cells in the presence of flow and proliferated at the same speed (Figures S1B and S1C). However, at later stages *in vitro*, single adhering bacteria of the $PilE_{SB}$ variant formed 3D, densely packed microcolonies on the cellular surface upon proliferation, whereas the $PilE_{SA}$ variant led to more dispersed, 2D microcolonies formed by a single bacterial monolayer and thus containing less bacteria (Figures S1D and S1E). *In vivo*, the aggregative capacity of bacteria did not affect survival in the blood of infected animals (Figure 1B). At the initial time points of infection (6 hr), aggregation had little effect on the ability of the bacteria to accumulate along vessels, but after 24 hr the non-aggregative strain showed a 60-fold decrease in bacteria number in the human skin compared to the aggregative one (Figure 1C). These results show that bacterial auto-aggregation is important for efficient late colonization of the endothelium and disease progression, underlining the ability of aggregates to highly deform in order to adapt to the complex geometry of the microcirculation.

N. meningitidis Aggregates Display a Viscous Liquid Behavior in Suspension

The above results raised the question of the physical mechanisms governing the formation and dynamics of *N. meningitidis* aggregates. Interestingly, several properties of aggregates formed *in vitro* were reminiscent of the behavior of liquid droplets. In liquid suspension, *N. meningitidis* cells spontaneously formed quasi-spherical, dynamic aggregates that tended to sediment to the bottom of the wells without adhering to the surface (Figures 2A and S2A; Video S1). In addition, when two aggregates came in close proximity, they rapidly fused and relaxed to a larger, spherical aggregate within a few minutes (Figures 2B and S2B–S2E; Video S1), suggesting that they can be described as a liquid phase endowed with an effective surface tension. This viscous liquid behavior was also corroborated by wetting experiments in which progressive aggregate spreading on an adhesive surface could be observed by total internal reflection fluorescence (TIRF) microscopy (Figures S2F–S2I). To quantify the mechanical properties of this phase, we adapted a micropipette aspiration protocol to our system (Guevorkian et al., 2010, 2011): the application of a constant negative pressure on a bacterial aggregate led to its deformation inside the micropipette (Figures 2C and 2D; Video S2). Interestingly, in the range of applied pressures (10–100 Pa), the length of the tongue linearly increased over time, indicating a purely viscous liquid behavior (Figure 2E). By analyzing the dynamics of the aggregates and further applying the Laplace law, we could obtain estimations of the aggregate viscosity (9 Pa.s) and surface tension at rest (0.1 mN/m) (Figures 2F and 2G). Thus, aggregates of *N. meningitidis* exhibit a liquid-like behavior with no elastic component even at short timescales. As a comparison, values of viscosity and surface tension for common viscous liquids can be found in Table S1. The viscosity of *N. meningitidis* aggregates is close to that of honey (2–10 Pa.s); however, its surface tension is much lower than that of honey (50–60 mN/m).

Diffusion of Bacteria inside the Aggregates Reaches Values Higher than Individual Bacteria in Suspension

To gain insights into the interactions driving this viscous behavior, we then moved to a smaller scale and characterized the motion of single fluorescently labeled wild-type (WT) bacteria inside aggregates, 30–40 μm in diameter, using spinning disk confocal imaging at high spatiotemporal resolution (Figures 3A, S3A, and S3B; Video S3). We characterized the movement of individual bacteria by an effective 2D diffusion coefficient, calculated based on the analysis of mean square displacements of single bacterial tracks over different time intervals, and consequent linear fit. This value integrates both phases of free diffusion and active pulling and provides a general characterization of bacterial motility within the aggregate. These results showed that diffusion coefficient was small for bacteria close to the aggregate center of mass (CM), and progressively increased with the distance from the center (d_{CM}) reaching maximal values at the aggregate periphery. The relationship between bacterial diffusion coefficient and distance to the center was confirmed over multiple aggregates (N = 20) after normalization for aggregate size (Figure 3B). The values of diffusion coefficients corresponding to a ~10-μm-thick outer layer (0.3–0.5 $\mu m^2/s$) exceeded the diffusion coefficient of single freely diffusing bacteria (Figures 3B and 3C). Diffusion of individual diplococci in suspension in liquid medium was determined experimentally to be 0.25 $\mu m^2/s$ and was not affected by piliation as a non-piliated strain (*pilD*) exhibited the same motility, consistently with the passive diffusive motion of a 1-μm-diameter particle in water. This feature stands in contrast to ordinary liquids at equilibrium, where attractive intermolecular forces ensure cohesion and slow down particle motion compared to the gas phase. In the case of *N. meningitidis* bacterial aggregates, we found on the contrary that individual bacteria within the aggregate (liquid phase) exhibit an apparent diffusion coefficient higher than non-interacting single bacteria outside of the aggregate (dispersed or gas-like phase). Pursuing the analogy with the movement of particles of a classical fluid in a liquid or dispersed phase, we concluded that this active system displays an anomalously fluidized phase, the origin of which deserves further clarification.

Pairwise Interaction between Bacteria Shows Cycles of Attraction and Release

To elucidate the origin of the unusual properties of *N. meningitidis* aggregates, we focused on the likely elementary building block of bacterial aggregation, i.e., the interactions between two cells. To this aim, we performed time-lapse microscopy of 2–10 isolated WT bacteria confined in quasi-2D circular microfabricated (width = 50 μm; height = 10 μm) agar chambers (Figure 4A). Bacteria were prevented from interacting with the glass substrate by passivation with a hydrophobic molecule (PLL-PEG), and no evidence of twitching motility could be observed in these conditions (Figures S3C and S3D). Bacteria diffused freely in the chambers, until two of them rapidly moved toward each other and got in close contact (Figure 4B; Video S4). After a variable contact time, bacteria detached and eventually resumed free diffusion or undertook a new phase of attraction, possibly with another cell. Detection of these "active pulling" events was implemented in a semi-automatic script based on the analysis of interbacterial distance and its first derivative as a function of time (Figure 4C). The active pulling events were T4P-dependent, since non-piliated bacterial mutants (e.g., *pilD*) failed to display them. Analysis of over 100 events

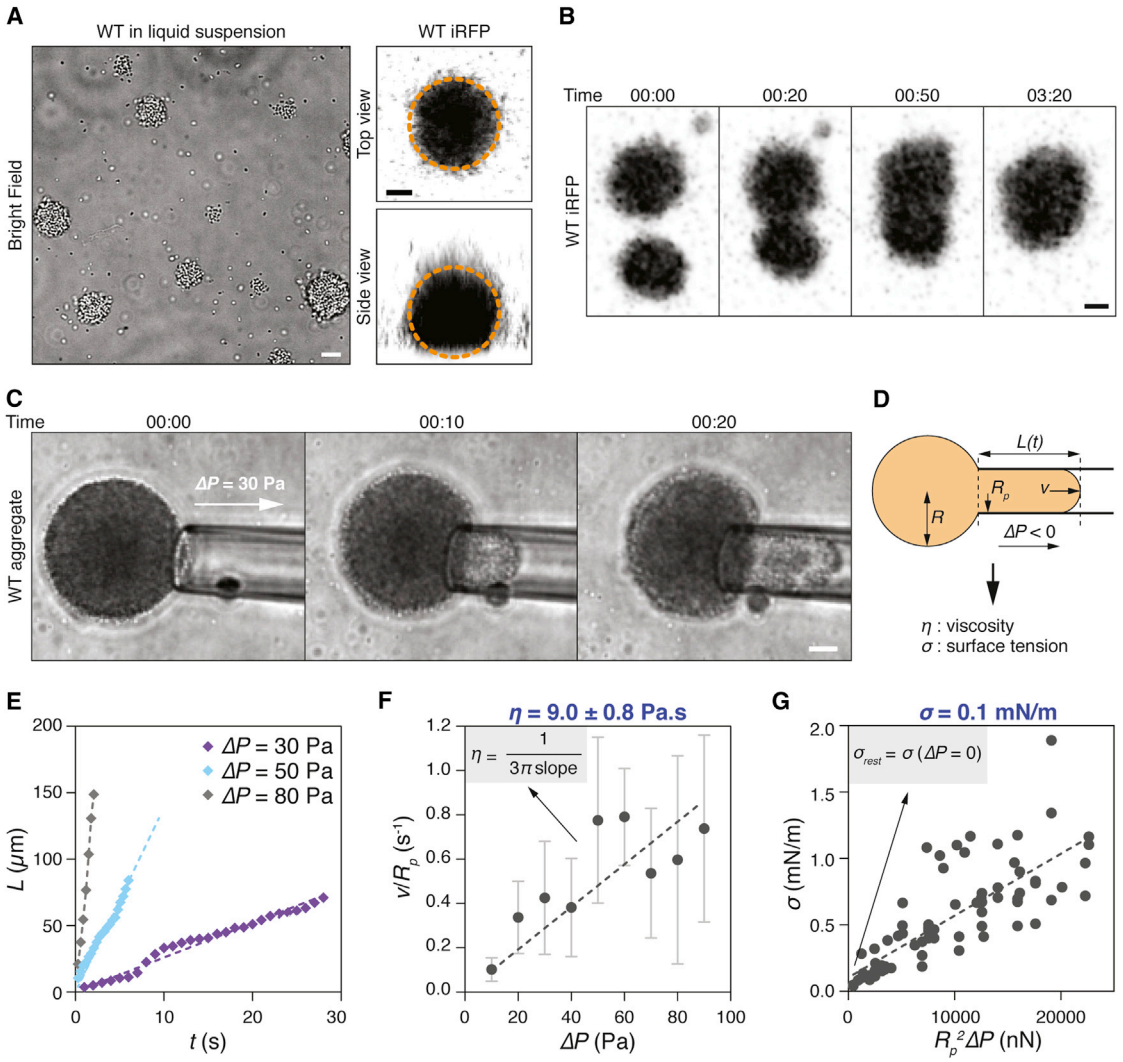

Figure 2. *N. meningitidis* Aggregates Display a Viscous Liquid Behavior in Suspension

(A) Left: bright-field image of WT bacterial aggregates. Right: top and side confocal views of a WT iRFP bacterial aggregate. The quasi-spherical aggregate shape in both views is highlighted by a dotted orange line. The plastic substrate was treated with PLL-PEG to minimize adhesion events. The image is representative of n = 3 independent experiments. Scale bars, 10 μm.

(B) Confocal time-lapse image of a fusion event between WT iRFP bacterial aggregates. Indicated times are in min:s. The image is representative of n = 3 independent experiments. Scale bar, 10 μm.

(C) Bright-field temporal evolution of a WT aggregate progressing into a micropipette upon aspiration (ΔP = 30 Pa). The image is representative of n = 3 independent experiments. Indicated times are in min:s. Scale bar, 10 μm.

(D) Schematic representation of micropipette aspiration and definition of physical parameters to estimate aggregate viscosity and surface tension. R, aggregate radius; R_p, pipette radius; $L(t)$, tongue length at instant t; ΔP, applied negative pressure; v, tongue progression speed in the pipette; η, aggregate viscosity; σ, aggregate surface tension.

(E) Aggregate progression inside the pipette (tongue length, L) as a function of time t upon application of 3 different pressures: 30, 50, and 80 Pa, indicated with violet, light-blue, and gray dots respectively. Curves are representative of n = 3 independent experiments. Dotted lines indicate corresponding linear fits used to estimate tongue progression speed.

(F) Tongue progression speed to pipette radius ratios for a range of applied pressures (10–100 Pa). Dots and error bars indicate corresponding average values and standard deviations for each applied pressure, ΔP. n = 3 independent experiments, N = 80 WT aggregates. A linear fit to extract aggregate viscosity is represented by a dotted line.

(G) Surface tension as a function of the applied force $R_p^2 \Delta P$. Dots indicate single surface-tension estimations for each aspiration event. Surface tension at rest is extrapolated with a linear fit (dotted line) at the corresponding null force. n = 3 independent experiments, N = 80 WT aggregates.

See also Figure S2, Table S1, and Videos S1 and S2.

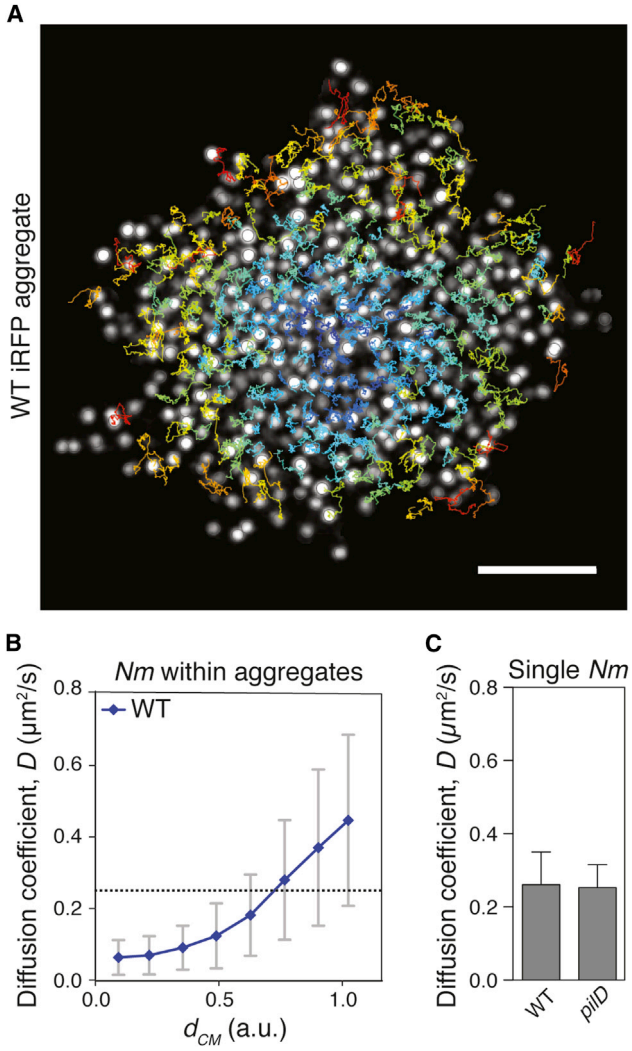

Figure 3. Diffusion of Bacteria inside the Aggregates Reaches Values Higher than Individual Bacteria in Suspension

(A) Single confocal slice of a WT iRFP aggregate in the middle plane and overlay of single bacterial tracks over a 10-s period with a 30-ms time step. Tracks are color-coded by their mean instantaneous speeds. The image is representative of n = 3 independent experiments. Scale bar, 10 μm.

(B) Average effective diffusion coefficients and corresponding standard deviations of individual bacteria as a function of their normalized distance from the aggregate center of mass, d_{COM} (0, center; 1; periphery). n = 3 independent experiments, N = 20 WT aggregates of similar size. The dotted line indicates the average diffusion coefficient of individual isolated WT bacteria.

(C) Average diffusion coefficients and corresponding standard deviations of individual bacteria for WT and the non-piliated mutant *pilD*. n = 3 independent experiments, N = 50 tracks/bacterial strain.

See also Figure S3 and Video S3.

of interacting bacteria provided a quantitative description of the elementary process initiating aggregation (Figures 4D–4G). For instance, mean interbacterial distance at the beginning of a pulling event was 6.9 μm but could reach up to 20 μm (Figure 4D). This is in agreement with previously reported measurements of average T4P length of the same strain by immunofluorescence (Imhaus and Duménil, 2014). Furthermore, a mean approaching speed of 1.5 μm/s (Figure 4E) during attraction sequences is in line with previous measurements using optical tweezers (Merz et al., 2000). Another signature of the attractive phase was given by the average interaction angle, defined as the angle between each single bacterial step and the axis intersecting the two bacteria, which was narrowly centered on 0 during interaction events underlining the high directionality of the mutual approach (Figure 4E, inset). Most importantly, and for the first time, this approach allowed to quantify the time intervals bacteria spent attracting each other (ON phase) or not (OFF phase) once they fall within the interaction range (20 μm). Probability distribution function of the ON and OFF phase durations followed an exponential decay with strikingly similar characteristic times, namely t_{ON} = 15.5 s and t_{OFF} = 16.3 s (Figures 4F and 4G). Analysis at the level of individual pairs of cells thus demonstrated an intermittent interaction process and provided the key parameters characterizing the T4P-mediated pairwise interaction between bacteria.

An Intermittent Attractive Force between Particle Pairs Is Sufficient to Recapitulate Aggregate Properties

The above results prompted us to investigate the role of intermittent attractive forces between bacteria as the physical basis of the highly fluidized phase formed by *N. meningitidis* aggregates. We hence built a 2D minimal model of active fluid in order to assess how an intermittent active process of rapid attraction between bacteria could relate to the overall unique material properties of aggregates (Method Details). Models have been previously used to describe the interaction of single *N. gonorrheae* cells with an abiotic surface (Marathe et al., 2014; Weber et al., 2015). Here, to analyze aggregation properties, we rather built and parameterized the model for numerical simulations focusing on the pairwise *N. meningitidis* bacterial interactions, characterized quantitatively in the micro-chambers (d_{int}, v_{int}, D, t_{ON} and t_{OFF}) (Method Details). Bacteria were modeled as apolar circular solid particles interacting via a pairwise potential with a hard-core repulsion reflecting the cell finite size. The T4P-dependent attachment and active pulling were modeled via an attractive force, which was stochastically turned ON and OFF for pairs of particles that were (1) within a cutoff distance (defined as the maximal distance at which two particles can interact, hence corresponding to twice the maximal pili length) and (2) neighbors, as defined by a Voronoi tessellation plane partitioning (Figure 5A). In effect, this restriction to Voronoi neighbors favored interactions within a first circle of an average of 6 neighbors, which corresponds to the experimentally determined average pili number per bacterium (Imhaus and Duménil, 2014). With these simple assumptions and experimentally determined parameters, simulated particles in a pair could undergo a cycle during which they attached, moved toward each other, remained in contact and finally detached (Figure 5B). At higher particle densities, initially randomly dispersed particles progressively organized in dynamic round-shaped aggregates that occasionally fused and formed a new larger and circular cluster, similarly to experimental data (Figure 5C). *In silico*-simulated large groups of particles displayed apparent diffusion coefficients in complete agreement with the experimental results of bacterial motion inside aggregates, remarkably requiring no

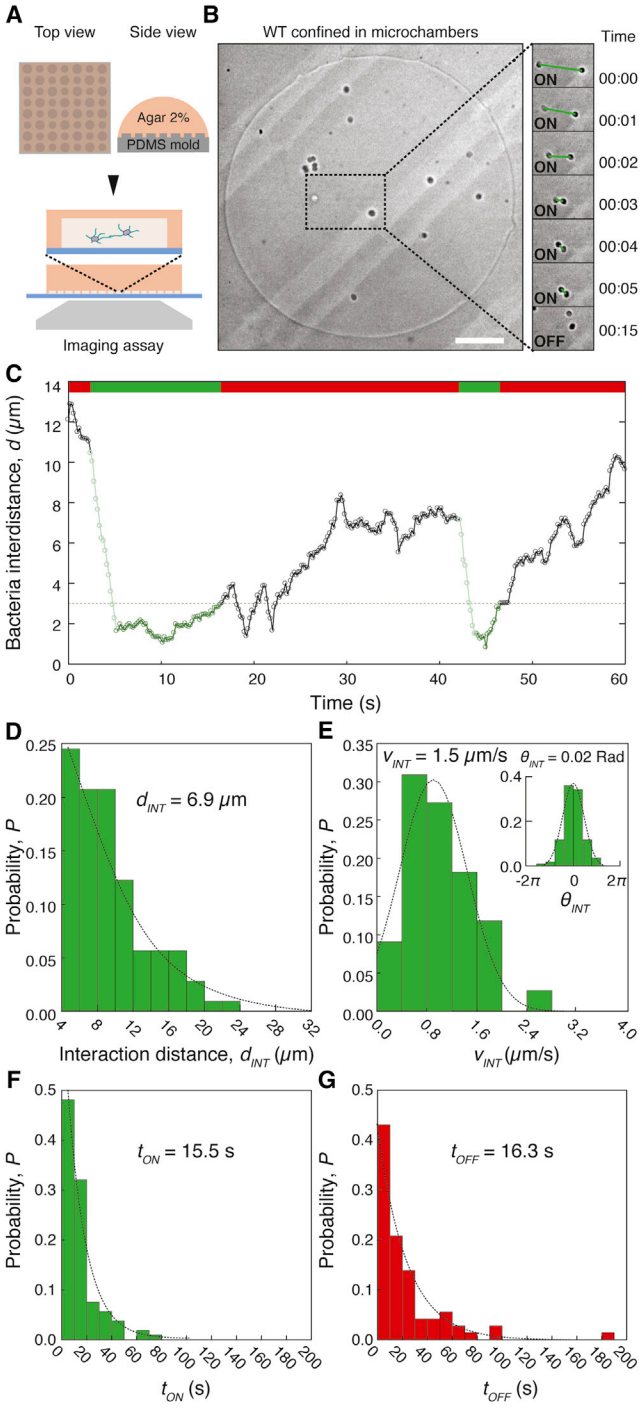

Figure 4. Pairwise Interaction between Bacteria Shows Cycles of Attraction and Release

(A) Schematic of agar chamber fabrication and experimental setup to observe the interaction of a controlled number of bacteria.

(B) Left: bright-field view of WT bacteria confined inside agar chambers. Right: zoomed-in view of a time-lapse sequence showing an event of attraction (indicated by a green line) and release between two bacteria. The image is representative of n = 3 independent experiments. Time is indicated in min:s. Scale bar, 10 μm.

parameter adjustment (Figure 5D). Moreover, the spatial distribution of diffusion coefficients was conserved, with low diffusion at the aggregate center and increasing values going outward, reaching values higher than free diffusion at the aggregate periphery (Figure 3K, dotted line). Aggregates of particles intermittently attracting each other thus exhibit a liquid-like behavior with high diffusion, confirming that the active intermittent interaction is sufficient to reproduce the highly diffusive fluidized phase of WT aggregates. A mean-field analysis complemented the numerical simulations of the model (Method Details). This analysis confirmed that the observed high diffusion properties can be attributed to the intermittent dynamics of the pili, and suggests the following mechanism: the intermittent interaction events experienced by a cell with its neighbors act as an active source of noise in the system, thereby increasing its diffusion coefficient. Intermittent attractive forces thus promote efficient aggregate formation combined with a fluidization effect due to high particle diffusion.

Intermittent Attractive Properties between Bacteria Define a Phase Diagram of Aggregation Phenotypes

The mean-field analysis of the model further predicts, based on scaling arguments, that aggregate material properties (solid, liquid, or gas/dispersed) are controlled by the ratio of the time spent in the OFF (no attraction) and the ON (attraction) phases (i.e., t_{OFF}/t_{ON}). We examined numerically this main prediction. Accordingly, aggregate simulations at constant t_{ON} = 15 s while modulating t_{OFF} led to different states of matter (Figure 6A; Video S5): a solid phase with frozen crystal-like aggregates for low values of t_{OFF}/t_{ON}, a liquid phase with dynamic aggregates with t_{OFF}/t_{ON}~*1* and finally a dispersed gas-like phase where no aggregates formed at high values of t_{OFF}/t_{ON}. To identify these phase transitions, we used the average particle diffusion coefficient in the aggregate to quantitatively determine solid-to-liquid transition, and the dynamic stability of large aggregates defined by the radius of gyration for the liquid-to-gas transition (Figure 6B, dark and light gray lines, respectively). Interestingly, these simulations indicate that the average diffusion coefficient curve peaked at a t_{OFF}/t_{ON} ratio equal to 1, very close to the value measured experimentally with WT bacteria (Figure 6B, dark-gray line). Importantly, particles in the

(C) Interbacterial distance measured as a function of time for the pair highlighted in Figure 3B. The interaction phases appear in green (with the attraction and contact sub-phases in light and dark green respectively), and the non-interacting phases appear in red. An arbitrary threshold of 3 μm for the interbacterial distance was chosen to define the end of the ON phase.

(D) Probability distribution histogram of measured interaction distances. A mean value is extracted with an exponential fit. n = 3 independent experiments, N = 100 interaction events.

(E) Probability distribution histogram of measured approaching speeds and angles (inset). Mean values are extracted with a Gaussian fit. n = 3 independent experiments, N = 100 interaction events.

(F) Probability distribution histogram of measured interaction times (t_{ON}). A mean value is extracted with an exponential fit. n = 3 independent experiments, N = 100 interaction events.

(G) Probability distribution histogram of measured non-interacting time while within the interaction range (t_{OFF}). A mean value is extracted with an exponential fit. n = 3 independent experiments, N = 100 interaction events.

See also Figure S3 and Video S4.

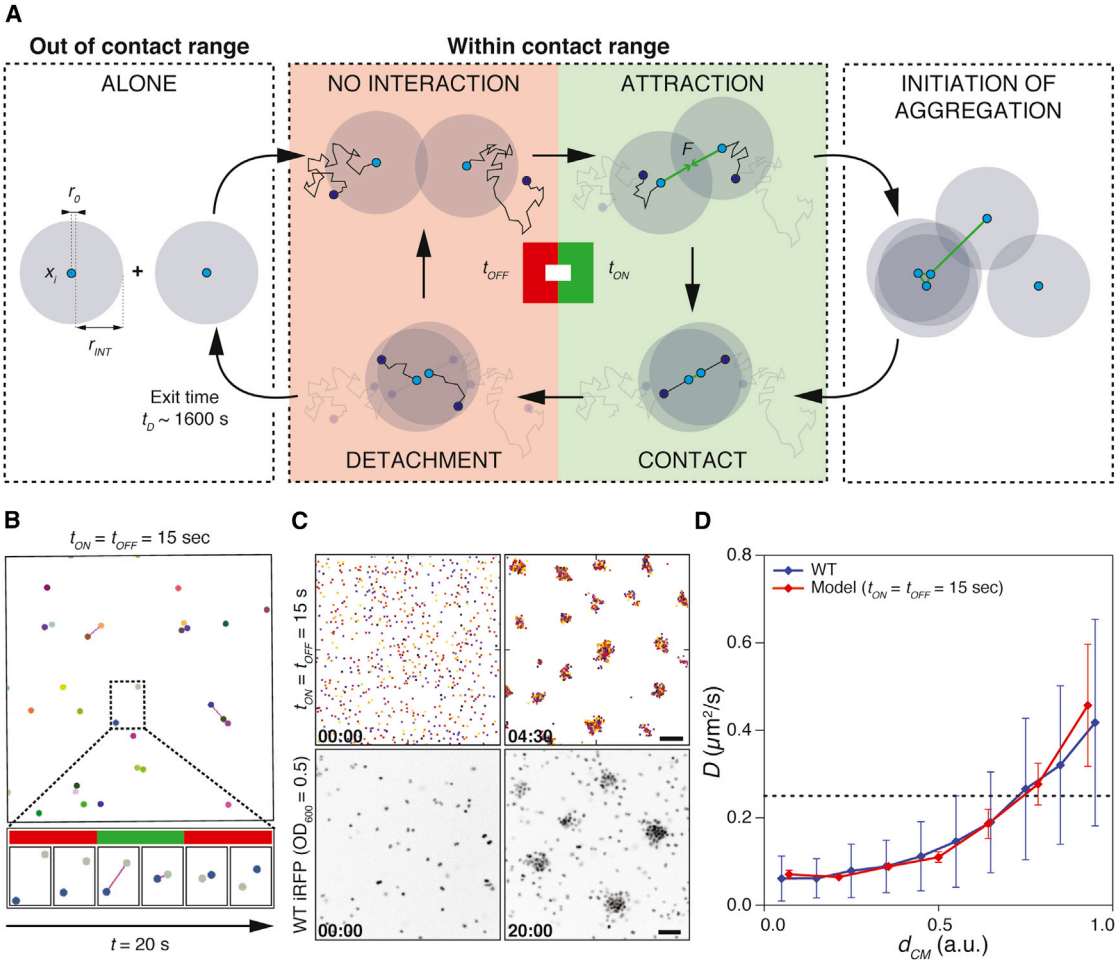

Figure 5. An Intermittent Attractive Force between Particle Pairs Is Sufficient to Recapitulate Aggregate Properties

(A) Schematic of the main physical principles implemented in the computational model of intermittent interaction. Individual particles are defined by a hard core (r_0) and an interaction range (r_{INT}). When the pair is within the interaction distance r_{INT}, it has a given probability of interaction (defined by t_{ON} and t_{OFF} characteristic times). During the interaction phase, an equal attractive force (F) is exerted on both particles bringing them together and keeping them in contact; finally, the force is released and particles detach and move away from each other. The exit time t_D corresponds to the time necessary for two particles to be out of range after contact by diffusion only. In the case of bacteria, $t_D \sim$1,600 s considering D = 0.25 $\mu m^2/s$ and a 20-μm maximum contact range.

(B) Top: view of simulated interactions between particles for $t_{ON} = t_{OFF}$ = 15 s. Bottom: zoomed-in view of a simulated time lapse showing interacting and non-interacting phases between two particles over 20 s, indicated in green and red, respectively.

(C) Top: simulation of aggregate formation dynamics starting from an initial random distribution, for $t_{ON} = t_{OFF}$ = 15 s and high particle density. Bottom: aggregate formation dynamics of WT iRFP bacteria at OD_{600} = 0.5. Time is indicated in min:s. Scale bars, 10 μm.

(D) *In vitro* and *in silico* effective diffusion coefficients of individual bacteria inside WT aggregates as a function of normalized distance from the aggregate center of mass (d_{CM}), indicated in blue and red, respectively. Simulated aggregates correspond to $t_{ON} = t_{OFF}$ = 15 s. Dots and error bars correspond to average values and standard deviations. The dotted line indicates the experimentally determined diffusion coefficient of isolated bacteria.

See also Figure S3.

external layer of the simulated aggregates showed a higher effective diffusion constant compared to individual particles (0.25 $\mu m^2/s$) thus recapitulating the high diffusion regime observed at the periphery of WT bacterial aggregates (Figure 6B, dark-gray, dashed line). Properties of T4P interaction corresponding to a t_{OFF}/t_{ON} ratio equal to 1, which were observed with WT bacteria, thus correspond to a maximum of intra-aggregate bacterial diffusion. Finally, we built up a complete phase diagram in the t_{ON} - t_{OFF} space by independently varying both parameters (Figure 6C). Numerical simulations were in agreement with mean-field analysis and showed that the actual balance between the time spent in the ON and OFF phases, the t_{OFF}/t_{ON} ratio, dictates the aggregative properties of the system (Method Details).

To complete the model validation, we tested its predictions by genetically manipulating bacteria. Slightly decreasing the t_{OFF}/t_{ON} ratio was predicted to strongly reduce intra-aggregate diffusion and thus increase viscosity (Figure 6D). *N. meningitidis* expresses a thick capsule at its surface composed of polymers of negatively charged sialic acid

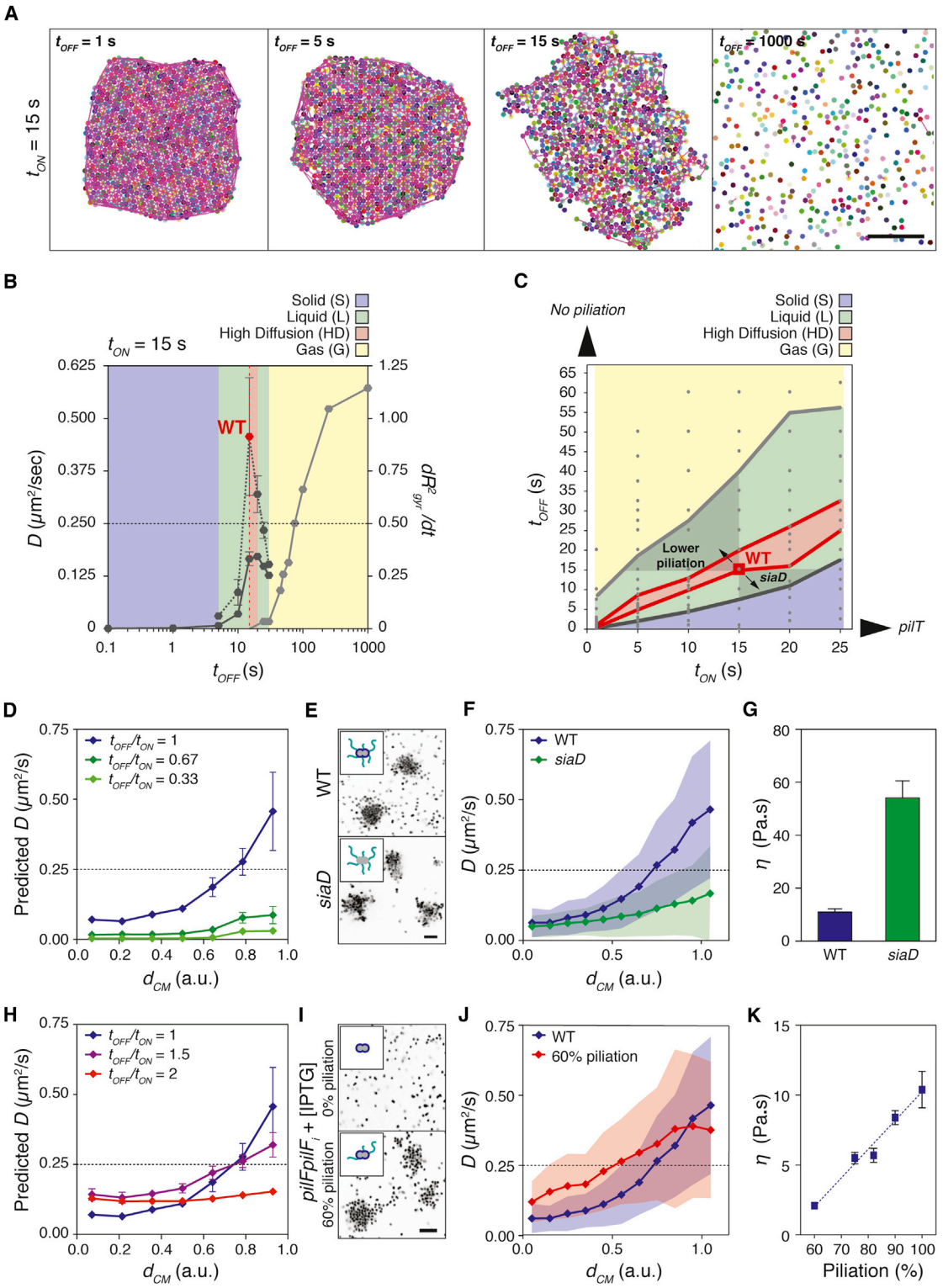

Figure 6. Intermittent Attractive Properties between Bacteria Define a Phase Diagram of Aggregation Phenotypes

(A) Views of *in silico* aggregation states for a fixed value of t_{ON} = 15 s and four different values of t_{OFF}: 1, 5, 15, and 1,000 s. Scale bar, 10 μm.

(B) Theoretical phase diagram of particle behavior as a function of t_{OFF} for a fixed value of t_{ON} = 15 s. Solid (blue) to liquid (green) transition is defined with the average diffusion coefficient of all particles in the aggregate (left axis, dark gray line). Liquid (green) to gas (yellow) transition is defined with the aggregate expansion rate, calculated as the derivative of square gyration radius (right axis, light gray line). The high diffusion zone (red) corresponds to a regime where the

(legend continued on next page)

residues in the serogroup C strain used here. Mutants devoid of capsule (*siaD*) were still able to form aggregates but became ''stickier'' than their WT counterparts, thus displaying larger contact times and a corresponding decrease in the t_{OFF}/t_{ON} ratio (Figures 6C and 6E; Video S6). The results corroborated the model predictions showing that a low t_{OFF}/t_{ON} ratio decreased the intra-aggregate bacterial diffusion and flattened the spatial distribution of the diffusion values (Figure 6F). Accordingly, micropipette measurements showed that non-capsulated mutants form more viscous aggregates (50 Pa.s) (Figure 6G). Symmetrically, a slight increase in the t_{OFF}/t_{ON} ratio was predicted to fluidize the aggregate core and hence to decrease the overall viscosity (Figure 6H). In particular, the spatial distribution of diffusion coefficients was predicted to progressively flatten by increasing t_{OFF}/t_{ON}, with simulated particles in the aggregate center being more motile while particles at the boundaries being less motile compared to the simulation of the WT case (Figure 6H). To increase t_{OFF}/t_{ON} in our biological system, we reduced the number of pili expressed by bacteria (Imhaus and Duménil, 2014) and hence decreased the probability of attraction. As predicted by the model, bacteria at 60% piliation level compared to WT exhibited a flattened distribution of effective diffusion coefficients within the aggregate (Figure 6J). Micropipette aspiration showed a linear relationship between the average number of pili per cell and the viscosity of the aggregate (Figure 6K). In conclusion, by experimentally varying the probabilities of attraction and separation between bacteria using genetics we could modulate the physical properties of the bacterial aggregates as predicted by the model. Remarkably, the specific properties of bacterial interactions in the unmodified WT *N. meningitidis* place it in the phase diagram in a narrow region prone to the formation of viscous liquid aggregates fluidized by high intra-aggregate diffusion.

Fluid-like Behavior of Aggregates Favors Colonization of Capillaries

We then asked whether this intermittent attractive force generating a fluidization effect of *N. meningitidis* aggregates could have a function in their capacity to invade capillaries. The viscous aggregates highlighted in our study are highly deformable and this could allow adaptation to the particular geometry of the microcirculation during bacterial proliferation. To test this hypothesis, we used a bacterial mutant that forms aggregates but fails to display intermittent attractive forces. The *pilT* mutant, lacking the ATPase responsible for pilus retraction, is able to form contacts through its abundant pili but fails to detach (Figure 7A). As predicted, *pilT* aggregates were not round in shape and did not flow into the pipette even at high aspiration pressures, and individual bacteria failed to diffuse in the aggregates indicating a solid material totally devoid of fluid properties (Figures 7A–7C; Video S6). To test the ability of aggregates to adjust to the capillary geometry following volume increase due to bacterial proliferation, we allowed *pilT* and WT bacteria to grow in 10 μm-wide PDMS (polydimethylsiloxane) channels to mimic capillary dimensions. WT aggregates grew in a continuous fashion while rapidly adjusting to the imposed channel geometry (Figure 7D; Video S8). Aggregate size increased over time due to cell proliferation and occasional aggregate fusion with neighboring colonies (Figure 7E). In contrast, the solid-like *pilT* colonies initially grew as WT until they filled up the whole channel section, increased bacterial density and then stopped growing. From these results, we conclude that the viscous properties of the aggregates allow the growing microcolony to adjust to physical constraints.

To further validate this hypothesis *in vivo*, we tested the behavior of aggregates inside human vessels using spinning disk confocal intravital imaging. After infection of grafted animals with either the WT or the *pilT* strains, time-lapses of bacteria

average diffusion coefficient of particles at the aggregate periphery (left axis, dark gray dotted line) exceeds the diffusion coefficient of isolated bacteria (black dotted line). Location of WT bacterial aggregates is indicated with a red dot and red dotted line.

(C) Theoretical phase diagram of particle behavior as a function of t_{ON} and t_{OFF}. The color-code is the same as that used in Figure 4B. Gray dots indicate all simulated conditions to assess phase transitions. Light-gray regions illustrate model predictions for lower (bottom-right region, corresponding to *siaD* mutant) or higher (top-left region, corresponding to underpiliated mutants) t_{OFF}/t_{ON} ratios. Non-piliated mutants are located at the extreme top left of the diagram, corresponding to infinite t_{OFF}/t_{ON} ratio. Hyperpiliated mutant with non-retractile T4P (*pilT*) is located at the extreme bottom right of the diagram, corresponding to null t_{OFF}/t_{ON} ratio.

(D) Simulated diffusion coefficient as a function of the position in the aggregate with decreasing t_{OFF}/t_{ON} ratios (1, 0.67, and 0.33). Dots and error bars indicate corresponding average values and standard deviations for n = 3 independent simulations.

(E) Top left: schematic of WT and non-capsulated *siaD* mutant. Right: corresponding views of iRFP-expressing aggregates for each strain. Images are representative of n = 3 independent experiments. Scale bar, 10 μm.

(F) Experimental measurement of the diffusion coefficient of individual bacteria as a function of their positon in the aggregate for WT (blue) and *siaD* (green). Average values and corresponding standard deviations are indicated with dots and filled regions, respectively. n = 3 independent experiments, N = 20 aggregates/bacterial strain.

(G) Viscosity of the *siaD* (green) mutant compared to WT (blue) as determined by micropipette aspiration. n = 3 independent experiments, N = 15 aggregates/bacterial strain. Average values and corresponding standard deviations are indicated for each condition.

(H) Simulated diffusion coefficient as a function of the position in the aggregate with increasing t_{OFF}/t_{ON} ratios (1, 1.5, and 2). Dots and error bars indicate corresponding average values and standard deviations for n=3 independent simulations.

(I) Top left: schematic of the *pilF* inducible strain with amounts of inducer generating 0% (top) and 60% (bottom) of piliation relative to WT. Right: corresponding view of iRFP-expressing bacteria for each condition. Images are representative of n = 3 independent experiments. Scale bar, 10 μm.

(J) Experimental measurement of the diffusion coefficient of individual bacteria as a function of their positon in the aggregate for WT (blue) and *pilF* inducible strain at 60% of piliation (red). Average values and corresponding standard deviations are indicated with dots and filled regions, respectively. n = 3 independent experiments, N = 20 aggregates/bacterial strain.

(K) Viscosity of the *pilF*-inducible strain treated with various levels of inducer and thus different levels of piliation as determined by micropipette aspiration. n = 3 independent experiments, N = 15 aggregates/bacterial strain. Average values and corresponding standard deviations are indicated for each condition.

See also Figure S3 and Videos S5 and S6.

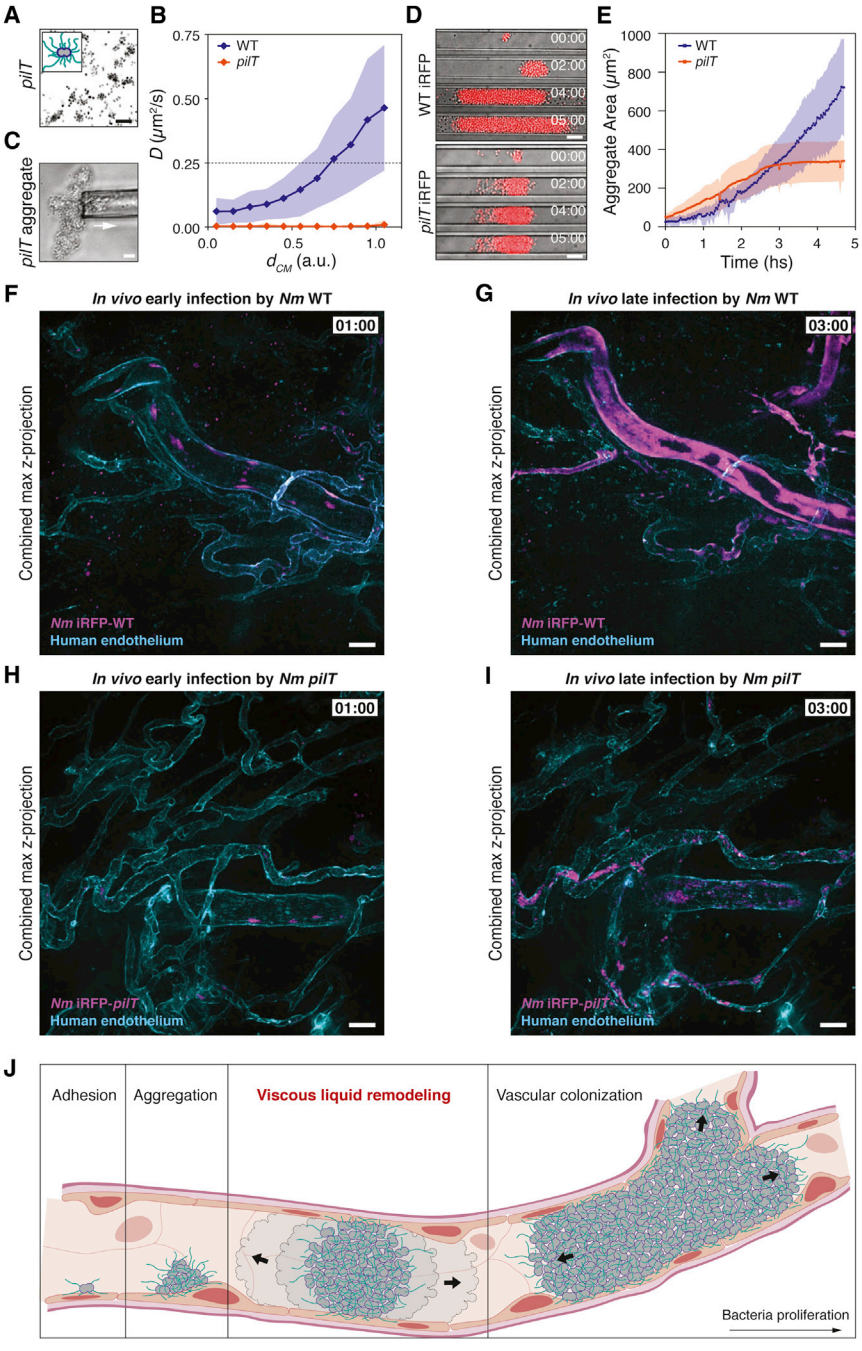

Figure 7. Fluid-like Behavior of Aggregates Favors Colonization of Capillaries

(A) Top left: Schematic of the *pilT* mutant. Right: Corresponding view of iRFP-expressing mutant aggregates. Images are representative of n = 3 independent experiments. Scale bar, 10 μm.

(B) Experimental measurement of the diffusion coefficient of individual bacteria as a function of their position in the aggregate for WT (blue) and *pilT* (orange). Average values and corresponding standard deviations are indicated with dots and filled regions, respectively. n = 3 independent experiments, N = 20 aggregates/bacterial strain.

(C) Bright-field view of a *pilT* aggregate subjected to micropipette aspiration but unable to deform and progress as a fluid. Images are representative of n = 3 independent experiments. Scale bar, 10 μm.

(D) Time-lapse combined view of iRFP-expressing proliferating WT and *pilT* aggregates inside 10-μm-wide PDMS microchannels. Bright field: gray; iRFP: red. Time indicated in hr:min. Images are representative of n = 3 independent experiments. Scale bar, 10 μm.

(E) Quantification of the surface of aggregates formed by WT (blue) and *pilT* (orange) inside microchannels following proliferation over a 5-hr period. Average values and corresponding standard deviations are indicated with dots and filled regions, respectively. n = 3 independent experiments, N = 15 aggregates/bacterial strain.

(F) Maximal intensity projection of human vascular network infected with the iRFP-expressing WT strain (magenta) 1-hr post-infection. The endothelium is labeled with UEA-1-lectin conjugated with AlexaFluor 750 (AF750) (cyan). Scale bar, 50 μm.

(G) Same as in (F), but 3 hr post-infection. Scale bar, 50 μm.

(H) Maximal intensity projection of human vascular network infected with the iRFP-expressing *pilT* strain (magenta) 1 hr post-infection. The human endothelium is labeled with UEA-1-lectin conjugated with AF750 (cyan). Scale bar, 50 μm.

(I) Same as in (H), but 3 hr post-infection. Scale bar, 50 μm. All *in vivo* images are representative of n = 6 independent experiments on N = 3 mice for each bacterial strain, with simultaneous acquisition of 5–6 fields of view in each experiment.

(J) Model of vascular colonization by *Nm* viscous liquid aggregates: viscous liquid properties of bacterial aggregates allow vascular colonization. Bacteria (indicated in gray) initially bind through T4P (indicated in green) as individuals and then proliferate eventually occluding the vessel lumen covered by endothelial cells (indicated in red), themselves wrapped in the basal lamina (indicated in purple). As bacteria continue to proliferate, the aggregate becomes mechanically constrained by the small diameter of the infected capillaries. At this stage, the viscous properties become essential to allow proliferating aggregates to adapt to the geometry of the vessels, leading to the large aggregates observed *in vivo*. See also Videos S7, S8, and S9.

colonization inside human vessels were acquired for a period of 3 hr (Figures 7F–7I; Video S9 and S10). After initial adhesion, the WT strain proliferated forming dense, fluid-like colonies that adapted to the vessel geometry, fused together, and progressively occupied the vascular lumen of vessels ranging from 10 to 50 μm in diameter (Figures 7F and 7G; Video S9). The progression of the aggregates as they increased in size inside the blood circulation exhibited a flowing motion reminiscent of a viscous fluid (Figure 7D). Similarly to the WT strain, the *pilT* mutant adhered efficiently to the vascular walls and formed small aggregates, but at later stages their size quickly reached a plateau and failed to occupy the vascular luminal space, even

of capillary-size vessels (Figures 7H and 7I; Video S10). To conclude, in the absence of viscous fluid properties, bacterial aggregates fail to adapt to the geometry of the capillary network and to fully colonize the vascular space.

DISCUSSION

Analysis of human cases as well as studies conducted with a humanized animal model revealed that aggregates of *N. meningitidis* were able to adapt to the shape of the infected vessels, reaching high aspect ratios and complex morphologies (Figure 7J). Here, we show that during infection bacterial aggregation is not only a side effect of proliferation but an active process because of the specific physical properties of *N. meningitidis* bacteria-bacteria interactions.

Beyond the simple property of sticking together, the viscous-like properties of the aggregates are a determining feature of the infection process. As bacteria proliferate, the environment of infected micro-vessels rapidly becomes a physical limit (Figure 7J). The ability of *N. meningitidis* bacterial aggregates to "flow" in the vascular lumen (Video S9), fuse with each other and quickly adapt to the vessel geometry through implementation of intermittent attractive forces could account for the exceptionally rapid disease progression of meningococcemia with rapid occupation of entire vascular networks and loss of organ function observed during *purpura fulminans*. Therefore, we unveil aggregate rheology as a novel potential target to be addressed by genetics and drug development for disease treatment. However, how this viscous liquid behavior could impact on other cellular players of the vascular network, such as endothelial cells, circulating cells, and coagulation components, remains an open question. Further studies also will be necessary to evaluate whether other pathogens display similar properties and their impact on disease progression. In *Neisseria gonorrheae*, for instance, a sorting phenomenon has been described upon changes in pilus posttranslational modifications highlighting a complex dynamics of aggregation in this species as well (Oldewurtel et al., 2015; Taktikos et al., 2015).

Liquid phases are increasingly recognized as important in biological processes at different scales, ranging from the molecular level to bacterial communities, ants aggregates up to penguin huddles (Brangwynne et al., 2009; Tennenbaum et al., 2016; Gilbert et al., 2008). For instance, small P granules in the *C. elegans* embryo exhibit liquid-like behaviors, including fusion and wetting, that structure the cytoplasm and regulate germline specification (Brangwynne et al., 2009). In the case of ants, contacts between legs are also intermittent and could thus engage similar mechanical and remodeling features as the ones studied here (Tennenbaum et al., 2016). Finally for penguin huddles, individuals progressively move around to alternate between a position in the middle of the group and on the outside where they are exposed to the cold (Gilbert et al., 2008). In particular, the external layer of the huddle is very dynamic, showing liquid-like movements reminiscent of our fluidized phase in Neisserial aggregates. The dynamics and/or mechanics of such groups of individuals can confer novel, unique features, such as a high resistance to stress. In the case of *N. meningitidis*, further studies are required to assess whether the viscous liquid behavior of aggregates could also lead to a better access to nutrients, and if this is genetically regulated for adaptation to different environments.

Our model of intermittent attractive interactions leading to aggregation is interestingly related—yet at another scale—to previous studies investigating actomyosin-based formation of cytokinetic nodes in the model organism fission yeast (Vavylonis et al., 2008). In that case, a growing actin filament has a certain probability to contact a myosin motor containing node from another filament, leading to a pulling force, contact between nodes, and cofilin-mediated final release. These transient connections would allow correct remodeling and assembly of the cytokinetic ring while avoiding formation of amorphous clusters. Hence, our system recapitulates—though at a larger scale—some of the main properties of actomyosin active meshworks. Furthermore, in a recent study successfully reconstituting search-capture-pull *in vitro*, a formin responsible of actin filament elongation was found to be a mechanosensor of myosin pulling forces, leading to inhibition of actin assembly (Zimmermann et al., 2017). Therefore, it will be of interest to investigate whether similar mechanosensing mechanisms are at play in T4P-mediated interactions of *N. meningitidis* and the consequences on bacterial aggregation.

Our study further revealed a unique type of viscous material comprising particles endowed with higher diffusion coefficients in the liquid phase than in the dispersed phase that is analogous to a gas phase in the textbook descriptions of the distinct states of matter. This is in contrast with the classical description of the gas phase, which is defined by a higher diffusion of particles as compared to the liquid phase. A mean-field analysis of our model suggests that this atypical high diffusion can be attributed to the intermittent dynamics of the interaction between particles, which acts as an additional source of noise in the system by increasing the diffusion coefficient of particles and therefore fluidizing aggregates. T4P-mediated interactions are therefore the source of both cohesion forces, which favor aggregate formation, and noise in cell dynamics, which favors aggregate fluidization. Importantly, these properties are shown to be critically controlled by the typical timescales $t_{ON} - t_{OFF}$ characterizing T4P dynamics in a non-trivial manner. A full analysis of the active noise and its consequences in an active, out-of-equilibrium system are left for future studies. In the context of infection, intermittent attractive forces between bacteria provide an optimum to combine efficient aggregation with a high diffusion required for low viscosity, leading to rapid adaptation to the geometry of blood capillaries during meningococcal infections. In addition to a better understanding of the physics behind the pathogenicity of *N. meningitidis*, our study uncovers novel design principles for materials with tunable viscosity.

STAR★METHODS

Detailed methods are provided in the online version of this paper and include the following:

- KEY RESOURCES TABLE
- CONTACT FOR REAGENT AND RESOURCE SHARING

- EXPERIMENTAL MODEL AND SUBJECT DETAILS
  - Mice and xenograft model of infection
  - Cell culture
  - Bacterial preparation
- METHOD DETAILS
  - Preparation of tissue samples immunohistochemistry
  - *Ex vivo* CFU enumeration
  - Bacterial growth experiments
  - Initial adhesion experiments and quantification
  - Bacteria proliferation experiments on HUVECs
  - Fusion experiments and quantification
  - Wetting experiments and quantification
  - Micropipette aspiration experiments and quantification
  - Single bacteria tracking in aggregates and quantification
  - Micro-chambers fabrication
  - Bacterial interactions experiments
  - Bacterial interactions quantification
  - Theoretical Model
  - Micro-channels fabrication
  - Micro-channels experiments and quantification
  - Spinning disk intravital microscopy
- QUANTIFICATION AND STATISTICAL ANALYSIS
- DATA AND SOFTWARE AVAILABILITY

SUPPLEMENTAL INFORMATION

Supplemental Information includes three figures, one table, and ten videos and can be found with this article online at https://doi.org/10.1016/j.cell.2018.04.010.

ACKNOWLEDGMENTS

Authors would like to thank Daiki Nishiguchi, Matthieu Piel and Ana-Maria Lennon-Duménil for fruitful discussions and critical reading of the manuscript. Authors would also like to acknowledge Samy Gobaa (Biomaterials and Microfluidics platform, Institut Pasteur) as well as Rafaele Attia and Jian Shi in Matthieu Piel's lab for technical advice and support in microfabrication; the animal facility of Institut Pasteur; Taliah Schmitt at the Hôpital Saint Joseph for providing the human samples for *in vivo* experiments. This work was supported by the Agence National de la Recherche (ANR-08-PCVI-0032, G.D.), the Fondation pour la Recherche Médicale (DEI20151234399, G.D. and H.C.), the Integrative Biology of Emerging Infectious Diseases (IBEID) laboratory of excellence (ANR-10-LABX-62), and a VIP European Research Council-starting grant (310790-VIP, G.D.). D.B. was funded by the 2015 Roux-Cantarini fellowship (Institut Pasteur) and the 2017 Lefoulon-Delalande fellowship (Collège de France).

AUTHOR CONTRIBUTIONS

This work represents the combined research directions of two groups (G.D. and R.V./H.C.). *In vivo* experiments were performed by S.M. and V.M. Video microscopy experiments of aggregate dynamics and microfabrication were performed by D.B. Micropipette aspiration experiments were performed by V.L.S., N.H., and J.H. Image analysis was performed by D.B. and H.T. Modeling was performed by I.D.-C. Intravital experiments were performed by P.N. All authors designed the experiments. D.B., G.D., H.C., and R.V. wrote the paper.

DECLARATION OF INTERESTS

The authors declare no competing interests.

Received: September 28, 2017
Revised: January 11, 2018
Accepted: April 10, 2018
Published: May 17, 2018

REFERENCES

Barrat, J.-L., and Hansen, J.-P. (2003). Basic Concepts for Simple and Complex Liquids (Cambridge University Press).

Biais, N., Ladoux, B., Higashi, D., So, M., and Sheetz, M. (2008). Cooperative retraction of bundled type IV pili enables nanonewton force generation. PLoS Biol. *6*, e87.

Brangwynne, C.P., Eckmann, C.R., Courson, D.S., Rybarska, A., Hoege, C., Gharakhani, J., Jülicher, F., and Hyman, A.A. (2009). Germline P granules are liquid droplets that localize by controlled dissolution/condensation. Science *324*, 1729–1732.

Brissac, T., Mikaty, G., Duménil, G., Coureuil, M., and Nassif, X. (2012). The meningococcal minor pilin PilX is responsible for type IV pilus conformational changes associated with signaling to endothelial cells. Infect. Immun. *80*, 3297–3306.

Budrene, E.O., and Berg, H.C. (1991). Complex patterns formed by motile cells of Escherichia coli. Nature *349*, 630–633.

Filonov, G.S., Piatkevich, K.D., Ting, L.M., Zhang, J., Kim, K., and Verkhusha, V.V. (2011). Bright and stable near-infrared fluorescent protein for in vivo imaging. Nat. Biotechnol. *29*, 757–761.

Gilbert, C., Blanc, S., Le Maho, Y., and Ancel, A. (2008). Energy saving processes in huddling emperor penguins: from experiments to theory. J. Exp. Biol. *211*, 1–8.

Guevorkian, K., Colbert, M.J., Durth, M., Dufour, S., and Brochard-Wyart, F. (2010). Aspiration of biological viscoelastic drops. Phys. Rev. Lett. *104*, 218101.

Guevorkian, K., Gonzalez-Rodriguez, D., Carlier, C., Dufour, S., and Brochard-Wyart, F. (2011). Mechanosensitive shivering of model tissues under controlled aspiration. Proc. Natl. Acad. Sci. USA *108*, 13387–13392.

Heuzé, M.L., Collin, O., Terriac, E., Lennon-Duménil, A.M., and Piel, M. (2011). Cell migration in confinement: a micro-channel-based assay. Methods Mol. Biol. *769*, 415–434.

Ho, M., Hickey, M.J., Murray, A.G., Andonegui, G., and Kubes, P. (2000). Visualization of plasmodium falciparum-endothelium interactions in human microvasculature: mimicry of leukocyte recruitment. J. Exp. Med. *192*, 1205–1211.

Imhaus, A.F., and Duménil, G. (2014). The number of Neisseria meningitidis type IV pili determines host cell interaction. EMBO J. *33*, 1767–1783.

Löwen, H. (1994). Melting, freezing and colloidal suspensions. Phys. Rep. *237*, 249–324.

Maier, B., Potter, L., So, M., Long, C.D., Seifert, H.S., and Sheetz, M.P. (2002). Single pilus motor forces exceed 100 pN. Proc. Natl. Acad. Sci. USA *99*, 16012–16017.

Mairey, E., Genovesio, A., Donnadieu, E., Bernard, C., Jaubert, F., Pinard, E., Seylaz, J., Olivo-Marin, J.C., Nassif, X., and Duménil, G. (2006). Cerebral microcirculation shear stress levels determine Neisseria meningitidis attachment sites along the blood-brain barrier. J. Exp. Med. *203*, 1939–1950.

Marathe, R., Meel, C., Schmidt, N.C., Dewenter, L., Kurre, R., Greune, L., Schmidt, M.A., Müller, M.J., Lipowsky, R., Maier, B., and Klumpp, S. (2014). Bacterial twitching motility is coordinated by a two-dimensional tug-of-war with directional memory. Nat. Commun. *5*, 3759.

Marchetti, M.C., Joanny, J.F., Ramaswamy, S., Liverpool, T.B., Prost, J., Rao, M., and Aditi Simha, R. (2013). Hydrodynamics of soft active matter. Rev. Mod. Phys. *85*, 1143.

Melican, K., Michea Veloso, P., Martin, T., Bruneval, P., and Duménil, G. (2013). Adhesion of Neisseria meningitidis to dermal vessels leads to local vascular damage and purpura in a humanized mouse model. PLoS Pathog. *9*, e1003139.

Merz, A.J., So, M., and Sheetz, M.P. (2000). Pilus retraction powers bacterial twitching motility. Nature *407*, 98–102.

Nassif, X., Lowy, J., Stenberg, P., O'Gaora, P., Ganji, A., and So, M. (1993). Antigenic variation of pilin regulates adhesion of Neisseria meningitidis to human epithelial cells. Mol. Microbiol. *8*, 719–725.

Oldewurtel, E.R., Kouzel, N., Dewenter, L., Henseler, K., and Maier, B. (2015). Differential interaction forces govern bacterial sorting in early biofilms. eLife *4*, 4.

Persat, A., Nadell, C.D., Kim, M.K., Ingremeau, F., Siryaporn, A., Drescher, K., Wingreen, N.S., Bassler, B.L., Gitai, Z., and Stone, H.A. (2015). The mechanical world of bacteria. Cell *161*, 988–997.

Pujol, C., Eugène, E., Marceau, M., and Nassif, X. (1999). The meningococcal PilT protein is required for induction of intimate attachment to epithelial cells following pilus-mediated adhesion. Proc. Natl. Acad. Sci. USA *96*, 4017–4022.

Rotman, E., and Seifert, H.S. (2014). The genetics of Neisseria species. Annu. Rev. Genet. *48*, 405–431.

Rusniok, C., Vallenet, D., Floquet, S., Ewles, H., Mouzé-Soulama, C., Brown, D., Lajus, A., Buchrieser, C., Médigue, C., Glaser, P., and Pelicic, V. (2009). NeMeSys: a biological resource for narrowing the gap between sequence and function in the human pathogen Neisseria meningitidis. Genome Biol. *10*, R110.

Schindelin, J., Arganda-Carreras, I., Frise, E., Kaynig, V., Longair, M., Pietzsch, T., Preibisch, S., Rueden, C., Saalfeld, S., Schmid, B., et al. (2012). Fiji: an open-source platform for biological-image analysis. Nat. Methods *9*, 676–682.

Soyer, M., Charles-Orszag, A., Lagache, T., Machata, S., Imhaus, A.F., Dumont, A., Millien, C., Olivo-Marin, J.C., and Duménil, G. (2014). Early sequence of events triggered by the interaction of Neisseria meningitidis with endothelial cells. Cell. Microbiol. *16*, 878–895.

Taktikos, J., Lin, Y.T., Stark, H., Biais, N., and Zaburdaev, V. (2015). Pili-induced clustering of N. gonorrhoeae Bacteria. PLoS ONE *10*, e0137661.

Tennenbaum, M., Liu, Z., Hu, D., and Fernandez-Nieves, A. (2016). Mechanics of fire ant aggregations. Nat. Mater. *15*, 54–59.

Van Kampen, N.G. (2007). Stochastic Processes in Physics and Chemistry North (Elsevier).

Vavylonis, D., Wu, J.-Q., Hao, S., O'Shaughnessy, B., and Pollard, T.D. (2008). Assembly mechanism of the contractile ring for cytokinesis by fission yeast. Science *319*, 97–100.

Weber, C.A., Lin, Y.T., Biais, N., and Zaburdaev, V. (2015). Formation and dissolution of bacterial colonies. Phys. Rev. E Stat. Nonlin. Soft Matter Phys. *92*, 032704.

Zimmermann, D., Homa, K.E., Hocky, G.M., Pollard, L.W., De La Cruz, E.M., Voth, G.A., Trybus, K.M., and Kovar, D.R. (2017). Mechanoregulated inhibition of formin facilitates contractile actomyosin ring assembly. Nat. Commun. *8*, 703.

STAR★METHODS

KEY RESOURCES TABLE

REAGENT or RESOURCE	SOURCE	IDENTIFIER
Bacterial Strains		
Neisseria meningitidis C8013	Nassif et al., 1993	N/A
Neisseria meningitidis C8013 GFP	Melican et al., 2013	N/A
Neisseria meningitidis $PilE_{SB}$ GFP	Nassif et al., 1993	N/A
Neisseria meningitidis $PilE_{SA}$ GFP	Nassif et al., 1993	N/A
Neisseria meningitidis C8013 iRFP	This paper	N/A
Neisseria meningitidis C8013 *pilD*	Rusniok et al., 2009	N/A
Neisseria meningitidis C8013 *pilD* iRFP	This paper	N/A
Neisseria meningitidis C8013 *siaD*	Brissac et al., 2012	N/A
Neisseria meningitidis C8013 *siaD* iRFP	This paper	N/A
Neisseria meningitidis C8013 *pilT*	Pujol et al., 1999	N/A
Neisseria meningitidis C8013 *pilT* iRFP	This paper	N/A
Neisseria meningitidis C8013 *pilF* $pilF_i$	Imhaus and Duménil, 2014	N/A
Neisseria meningitidis C8013 *pilF* $pilF_i$ iRFP	This paper	N/A
Biological Samples		
Patient-derived xenografts (PDX)	Hôpital Saint Joseph	N/A
Chemicals, Peptides, and Recombinant Proteins		
GCB-Agar	Difco	CAT# 218091
RPMI 1640 medium	GIBCO	CAT# 11544526
Human endothelial-SFM medium (Endo-SFM)	GIBCO	CAT# 11540386
Fetal Bovine Serum (FBS)	PAA Laboratories	CAT# 11573397
Endothelial cells growth supplement (ECGS)	Alfa Aesar	CAT# 356006
Isopropyl β-D-1-thiogalactopyranoside (IPTG)	Sigma-Aldrich	CAS# 367-93-1
Ulex europaeus agglutinin (UEA) lectin - rhodamine	Vector Laboratories	CAT# DL-1067
Human Fibronectin	Sigma-Aldrich	CAT# F2006
FITC-conjugated lectin from *Triticum Vulgaris*	Sigma-Aldrich	CAT# L4895
PLL(20)-g[3.5]-PEG(2)	Surface Solutions	N/A
Experimental Models: Cell Lines		
Human umbilical vein endothelial cells (HUVEC)	Promocell	CAT# C-12200
Experimental Models: Organisms/Strains		
Humanized SCID/Beige (SOPF/CB17 SCID BEIGE. CB17.Cg-Prkdc-Lyst/Crl) mice	(Charles River, France)	Strain code: 250
Software and Algorithms		
Fiji	NIH	https://imagej.net/Fiji/Downloads RRID: SCR_002285
Metamorph Imaging Software	Molecular Devices	https://www.moleculardevices.com/products/cellular-imaging-systems/acquisition-and-analysis-software/metamorph-microscopy RRID: SCR_002368
MATLAB	MathWorks	https://www.mathworks.com/downloads/ RRID: SCR_001622
Huygens	Scientific Volume Imaging	https://svi.nl/Download
Prism	GraphPad Software	https://www.graphpad.com/scientific-software/prism/ RRID: SCR_002798

CONTACT FOR REAGENT AND RESOURCE SHARING

Further information and requests for resources and reagents should be directed to and will be fulfilled by the Lead Contact, Guillaume Duménil (guillaume.dumenil@pasteur.fr).

EXPERIMENTAL MODEL AND SUBJECT DETAILS

Mice and xenograft model of infection

5-8 weeks old SCID/Beige (SOPF/CB17 SCID BEIGE. CB17.Cg-Prkdc-Lyst/Crl) mice (Charles River, France), both males and females, were grafted with human skin as described in earlier studies (Melican et al., 2013) and used in all *in vivo* experiments. Briefly, split thickness grafts were prepared from human skin resulting from plastic surgery (Hôpital Saint Joseph, Paris, France) of adult individuals, both males and females without distinction, of various age (20-60 years old). Under anesthesia, a graft bed was prepared by excising an area of skin approximately 1–2 cm^2. Human skin was immediately placed over the graft bed and fixed in place with surgical glue (Vetbond, 3M, USA). Dressings were applied for 2 weeks and the graft was allowed to heal for 3 weeks. At this stage, human functional dermal microvasculature is present in the graft without inflammation. Prior to infection, mice were injected intraperitoneally with 8 mg of human transferrin (Sigma Aldrich). Mice were infected by intravenous injection of 100 μl 10^8 CFU/ml bacterial culture (10^7 CFU total). Mice were housed under a specific pathogen-free facility at Institut Pasteur. Mice were kept under standard conditions (light 07.00–19.00 h; temperature 22 ± 1°C; humidity 50 ± 10%) and fed autoclaved rodent feed and water *ad libitum*. The procedures described here for human skin xenografting and infection are very robust and reproducible, and no influence of mice sex on bacterial colonization have been observed (data not shown). All experimental procedures involving animals were conducted in accordance with guidelines established by the French and European regulations for the care and use of laboratory animals (Décrets 87–848, 2001–464, 2001–486 and 2001–131 and European Directive 2010/63/UE) and approved by the local ethical committee Comité d'Ethique en Expérimentation Animale n° 89, Institut Pasteur, Paris, France. No: 2015-0025. All surgery was performed under anesthesia, and all efforts were made to minimize suffering. For human skin, written informed consent was obtained and all procedures were performed according to French national guidelines and approved by the local ethical committee, Comité d'Evaluation Ethique de l'INSERM IRB 00003888 FWA 00005881, Paris, France Opinion: 11–048.

Cell culture

Primary human umbilical vein endothelial cells (HUVECs, Promocell) were used between passages 3 and 10 and grown at 37°C in a humidified incubator under 5% CO_2 in human endothelial-SFM (Endo-SFM, GIBCO) supplemented with 10% heat-inactivated fetal bovine serum (FBS, PAA Laboratories) and 10 μg/ml of endothelial cell growth supplement (ECGS, Alfa Aesar). Several batches of cells originating from multiple donors were used, from male and female donors with the same results.

Bacterial preparation

All *N. meningitidis* strains described in this study were derived from the recently sequenced 8013 serogroup C strain (http://www.genoscope.cns.fr/agc/nemesys) (Rusniok et al., 2009). Strains were streaked from −80°C freezer stocks onto GCB agar plates (Difco), and grown overnight in a moist atmosphere containing 5% CO_2 at 37°C. For all experiments, bacteria were transferred to liquid cultures in pre-warmed RPMI medium (GIBCO) supplemented with 10% FBS at adjusted OD_{600} = 0.05, and incubated with gentle agitation for 2 hours at 37°C in the presence of 5% CO_2. The *pilF pilF$_i$* strain was plated on GCB plates and then cultured in liquid media both containing IPTG in a range of 0 to 100 μM concentrations, depending on the level of piliation needed (Imhaus and Duménil, 2014). Natural variants in the pilin gene, namely $PilE_{SA}$ and $PilE_{SB}$ strains, have been previously described (Nassif et al., 1993) and were fluorescently labeled by cloning the gene encoding GFP under the control of the pilE gene promoter. Mutations in *pilD* (Rusniok et al., 2009), *siaD* (Brissac et al., 2012), *pilT* (Pujol et al., 1999) genes have been previously described. A plasmid allowing stable expression of the iRFP near-infrared fluorescent protein (Filonov et al., 2011) in *N. meningitidis*, pMGC13, was constructed as follows: the sequence encoding the iRFP protein was PCR-amplified from the plasmid pBAD/His-B-iRFP (a kind gift from Vladislav Verkhusha, Addgene plasmid #31855) with PacI and SalI restriction sites in 5′ and 3′ respectively and the ribosome binding site from *Nm pilE* gene just upstream of the start codon. The sequences for the primers are iRFP_F2: TTAATTAAAGGAGTAATTTTA TGGGGGGTTCTCATCATCATCA and iRFP_R3: GTCGACTCACTCTTCCATCACGCCGATCTGC (with restriction sites underlined and RBS from *pilE* in italic). The PCR fragment was then cloned in a pCRII-TOPO vector (Invitrogen), checked for sequence and subcloned in the pMGC5 plasmid that allows homologous recombination at an intergenic locus of the *Nm* chromosome and expression under the control of the constitutive *pilE* promoter (Soyer et al., 2014).

METHOD DETAILS

Preparation of tissue samples immunohistochemistry

Tissues were fixed 6 hs post infection with GFP-expressing bacteria in 4% paraformaldehyde (PFA), frozen in OCT (Tissuetek) and sliced into 10 μm-wide fragments. Immunofluorescence was performed using Mouse on Mouse detection kit (Vector laboratories). *Ulex europaeus* agglutinin-1 (UEA-1) lectin coupled to rhodamine (Vector laboratories) was used to stain human vessels. Samples

were mounted in Vectashield mounting reagent (Vector laboratories). Fluorescent images were acquired at 100 x magnification on an inverted spinning-disk confocal microscope (Ti-eclypse, Nikon) with a EMCCD camera (Evolve, Photometrics) using Metamorph Imaging Software (Molecular Devices). Images were post-processed using Fiji software (Schindelin et al., 2012).

Ex vivo CFU enumeration

Mice were sacrificed at different time points post infection (5 min and 6, 12, 24 hr). Human skin homogenates were obtained by cutting a 4 mm x 4 mm skin biopsy specimen from the xenograft and bacteria were isolated after homogenization using a MagNA Lyser homogenizer (Roche) in PBS. *Ex vivo* CFU were counted after plating serially diluted skin tissue homogenates overnight on GCB plates containing appropriate antibiotics. The same procedure was performed for CFU counting of blood samples. Data were analyzed on Prism software.

Bacterial growth experiments

Bacterial pre-cultures were diluted at initial OD_{600} = 0.05, loaded in a 96 well plate and incubated in a micro-plate reader (Cytation5, Biotek) under agitation at 37°C in the presence of 5% CO_2, with automated OD_{600} acquisition every 30 minutes for 18 hr. Data were analyzed on Prism software.

Initial adhesion experiments and quantification

Laminar flow experiments were performed as previously described (Mairey et al., 2006). Briefly, HUVECs were plated on 8-mm-diameter wells on glass slides coated with fibronectin (10 μg/ml) at a density of 10^4 cells/well. Cells grown on glass slides were placed in a parallel plate flow chamber and vacuum sealed. Experiments using the flow chamber were performed in Endo-SFM supplemented with 2% FBS at 37°C. Bacterial pre-cultures were diluted to OD_{600} = 0.075 and introduced into the chamber using a syringe pump (Vial Medical, Becton Dickinson, or Harvard Apparatus) at a shear stress of 0.044 dynes/cm^2. After 10 minutes of flow application, adherent bacteria were automatically detected and counted for multiple fields of view in the case of the pilin variants $PilE_{SA}$ and $PilE_{SB}$. Adhesion of bacteria was recorded using an Olympus CKX41 inverted microscope with a 20 x objective, equipped with a Hamamatsu ORCA285 CCD camera. A dedicated semiautomatic program was developed to detect, count, and track adherent *N. meningitidis* cells from fluorescence images.

Bacteria proliferation experiments on HUVECs

Time-lapse experiments were performed in Endo-SFM supplemented with 10% FBS at 37°C 5% CO_2. HUVECs were seeded into Ibidi μ-slides with Ibidi-treated plastic bottom (Ibidi) at a density of 10^4 cells/channel. Bacterial pre-cultures were diluted to OD_{600} = 0.02 (MOI = 200), loaded into the channels for 15 minutes at 37°C 5% CO_2 to allow bacterial adhesion and finally washed 3X with fresh medium. Time-lapse movies of GFP expressing $PilE_{SA}$ and $PilE_{SB}$ bacterial strains proliferating on HUVECs were acquired at 37°C 5% CO_2 on an inverted spinning-disk confocal microscope (Ti-eclypse, Nikon) over 4hs with a 20 x magnification, by coupling phase contrast and laser illumination (λ_{exc} = 488 nm). High resolution z stacks of bacterial colonies were performed on the same microscope with a 100 x magnification (z-step = 0.2μm). Images were acquired with a EMCCD camera (Evolve, Photometrics) using Metamorph Imaging Software (Molecular Devices). Image processing was performed using Fiji software (Schindelin et al., 2012).

Fusion experiments and quantification

Bacterial aggregates from a 2 hr pre-culture in RPMI + 10% FBS were loaded in a μ-dish chamber (Ibidi). Mineral oil was added on top to avoid evaporation. A micropipette was introduced in the chamber and used to put in close proximity aggregates with similar sizes to facilitate the fusion. Bright-Field and fluorescence time-lapses of fusion events were acquired with a 20 x magnification at 37°C 5% CO_2 on an inverted spinning-disk confocal microscope (Ti-eclypse, Nikon) at 0.2 fps for 2 minutes. To characterize the fusion dynamics, the temporal evolution of the contact surface between aggregates was quantitated via kymographs. Images were acquired with a EMCCD camera (Evolve, Photometrics) using Metamorph Imaging Software (Molecular Devices). Image processing and analysis were performed using Fiji software (Schindelin et al., 2012).

Wetting experiments and quantification

Glass substrates of CellView cell culture slides (Greiner) were plasma activated and coated with 100 μg/ml FITC-conjugated lectin from *Triticum Vulgaris* (Sigma-Aldrich, L4895) to allow bacterial adhesion. iRFP-expressing bacterial aggregates from a 2hs pre-culture in RPMI + 10% FBS were loaded and fast time-lapse acquisition at 100 x magnification was started to selectively visualize the temporal evolution of the aggregate contact area with the substrate over 20 minutes. Imaging was performed at 37°C 5% CO_2 on an inverted spinning-disk confocal microscope (Ti-eclypse, Nikon) equipped with a laser-based iLas2 total internal reflection fluorescence microscopy (TIRF) module (Roper Scientific) with a 647 nm laser and an ORCA03 digital CCD camera (Hamamatsu) by using Metamorph Imaging Software (Molecular Devices). Image processing and analysis were performed using Fiji software (Schindelin et al., 2012).

Micropipette aspiration experiments and quantification

Micropipette aspiration was largely performed as previously described (Guevorkian et al., 2010). Pipettes were fabricated by pulling borosilicate capillaries (1mm/0.78mm O/I diameter, Harvard Apparatus) with a laser-based puller (P-2000, Sutter Instruments). and sized to the desired diameter and fire-polished by using a microforge with a heated glass ball, to generate a smooth glass surface. Finally, the pipette tip was slightly bent by heating it with a flame, in order to minimize the angle between the pipette and the bottom of the observation chamber. A liquid suspension of bacterial aggregates was transferred to a tissue culture treated plastic Ibidi μ-dish (Biovalley, France) with walls cut to facilitate the access of the micropipette. Aggregates were then suspended in 600 μl of RPMI + 10% FBS and the open end was sealed with mineral oil to prevent evaporation. The micropipette was eventually introduced into the chamber. A range of pressures (ΔP = 10-100 Pa) was attained by vertically displacing a water reservoir, connected to the pipette, with respect to the observation chamber. Bright-Field movies of the progression of aggregates inside the pipette were recorded at 37°C 5% CO_2 on an inverted spinning-disk confocal microscope (Ti-eclypse, Nikon), with a frame rate of 10 images/s. Images were acquired with a EMCCD camera (Evolve, Photometrics) using Metamorph Imaging Software (Molecular Devices). Image processing and analysis were performed using Fiji software (Schindelin et al., 2012).

Single bacteria tracking in aggregates and quantification

Plastic bottom micro-channels (Ibidi) were passivated upon plasma activation and 30 min incubation with 0.1 mg/ml PLL(20)-g[3.5]-PEG(2) (Surface Solutions) solution in 10mM HEPES pH 7.4. Bacteria from 2hs pre-cultures in RPMI + 10% FBS and various concentrations of IPTG if needed, were then loaded in microchannels (Ibidi) and allowed to settle for 15 minutes at 37°C. Streaming movies of 10-20 s (time frame 30 ms) of iRFP-expressing bacteria were acquired at 37°C 5% CO_2 on an inverted spinning-disk confocal microscope (Ti-eclypse, Nikon) with 100 x magnification at the confocal middle plane using aggregates of similar sizes (30-40 μm in diameter) for the different conditions. Images were acquired with a EMCCD camera (Evolve, Photometrics) using Metamorph Imaging Software (Molecular Devices). Movies were post-processed with a standardized protocol on Fiji software, comprising background subtraction, Gaussian blurring and masking to define the aggregate contour (Schindelin et al., 2012). Single bacteria tracking was performed also on Fiji with Trackmate plugin. Analysis of bacterial tracks was performed with a custom-built script in MATLAB: briefly, average distance from the aggregate center of mass and mean square displacements (MSD) were calculated over each single bacterial track. Diffusion coefficients were extracted with a linear fit on the initial portion (10%) of the MSD curve. Aggregate size was normalized to 1 in order to obtain a cumulative distribution of diffusion coefficients over multiple aggregates (N = 20). Data were binned to extract average values and corresponding standard deviations in different aggregate regions.

Micro-chambers fabrication

Masters containing round micro-pillars of different sizes were fabricated using conventional positive photolithography techniques. The designs of the brass master molds were created using Clewin software. Briefly, a silicon wafer (Neyco S.A. France; diameter = 4-inch, thickness = 525) was spin-coated with TI Prime adhesion promoter (Microchemicals) and resist AZ® 9260 (Microchemicals). Predesigned features were patterned through a mask aligner (MJB4, Süss Microtec ReMan GmbH, Germany) equipped with an I-Liner filter (365nm) and a chuck for 4-inches wafers. The non-exposed resist was removed by solvent AZ® 400K in water solution, air-dried and passivated by overnight exposure to Trichloro(1H,1H,2H,2H-perfluorooctyl)silane vapors (Sigma Aldrich, ref: 448931). A 10:1 mixture of PDMS Sylgard 184 or RTV614 silicone elastomer and curing agent was poured onto the brass master and cured at 65°C for 3 hr.

Bacterial interactions experiments

PMDS chips were cleaned with isopropanol before a 30 s exposure to air plasma for activation. Agarose micro-chambers were prepared by pouring molten 2% agarose containing FITC-Dextran (MW 15 kD; Life Technologies) onto the PDMS chip. The agar pad was then stripped off, flipped and resized to a final 5 mm X 5 mm thick pad. Cells at OD600∼0.3 were diluted 20-fold, and 2 μL of bacterial suspension were loaded onto the agarose pad. As soon as the agar surface appeared dry, the pad was flipped onto a plastic bottom Fluorodish (Ibidi) previously passivated upon plasma activation and 30 min incubation with 0.1 mg/ml PLL(20)-g[3.5]-PEG(2) (Surface Solutions) solution in 10mM HEPES pH 7.4. Streaming movies of single iRFP-expressing WT bacteria diffusing in the micro-chambers were acquired at 37°C 5% CO_2 on an inverted spinning-disk confocal microscope (Ti-eclypse, Nikon) with 40 x magnification at 200 ms time frame for 3-5 minutes Images were acquired with a EMCCD camera (Evolve, Photometrics) using Metamorph Imaging Software (Molecular Devices).

Bacterial interactions quantification

Single bacteria tracking was performed on Fiji (Schindelin et al., 2012) with Trackmate plug-in and post-processed with a custom-made MATLAB script. We defined the 2 states of interactions between bacterial pairs as follows: (i) Attraction phase (or ON): this combines the active period where cells approach toward each other in a highly ballistic manner with a high speed, and the following contact period where bacteria remain in close proximity (cell-cell distance below threshold of 3 μm); (ii) No interaction phase (or OFF): corresponds to the time period where bacteria do not interact, e.g., they diffuse freely and are not in close proximity (cell-cell above threshold of 3 μm).

The approach phase was defined by characterizing the time-evolution of cell-cell distance as follows. First, we compute the relative cell-cell position $\vec{X}_3(t)$ and distance $L(t)$ as:

$$\vec{X}_3(t) = \vec{X}_1(t) - \vec{X}_2(t),$$

$$L(t) = \left|\vec{X}_3(t)\right|,$$

where $\vec{X}_1(t)$ and $\vec{X}_2(t)$ denote the 2D positions at instant t of bacterium 1 and 2 respectively. Their time derivatives, relative velocity $\vec{V}(t)$ and rate of distance change $\dot{L}(t)$, were defined as:

$$\vec{V}(t) = \frac{\left(\vec{X}_3(t+\tau/2) - \vec{X}_3(t-\tau/2)\right)}{\tau},$$

$$\dot{L}(t) = \frac{(L(t+\tau/2) - L(t-\tau/2))}{\tau},$$

where τ = 6 frames = 1.2 s.

The approach phases are characterized by a fast, ballistic approach of two bacteria, where cell-cell relative distance decreases rapidly. These phases were automatically detected by adopting two criteria:

(1) Approach phases correspond to a sharp decrease of $\dot{L}(t)$ to large negative values followed by its increase back to ~ 0; therefore, they should contain a local minimum of $\dot{L}(t)$.
(2) $\dot{L}(t)$ at the local minimum should be smaller than a threshold value, ***Thr*1**. ***Thr*1** was set to be -2.5 μm/s. This principle is necessary to distinguish true approach phases from other random non-directed motions.

The beginning and the end of a single approach phase were defined as the time points where $\dot{L}(t)$ exceeds a second threshold *Thr*2. *Thr*2 was set to be -1 μm/s.

The approach dynamics was characterized by computing the approach speed and orientation. The approach speed was defined as the norm of relative velocity:

$$\vec{V}_{INT}(t) = \left|\vec{V}(t)\right|,$$

The approach orientation θ_{INT} was defined as the orientation of $\left|\vec{V}(t)\right|$:

$$\theta_{INT} = tan^{-1}\left(\vec{V}(t) - \vec{X}_3(t)\right).$$

Note that if two bacteria are approaching straightly, θ_{INT} is 0 and approach speed is equal to $\dot{L}(t)$. Average speed and velocity orientation were defined as temporal averages for the entire period. Finally, analyses of all interaction events between bacterial pairs were pulled together to generate probability distributions of each parameter. Mean values of interaction distance, time of interaction (t_{ON}) and time of non-interaction (t_{OFF}) were derived by exponential fits, while mean values of interaction speed and interaction angle were derived by Gaussian fits.

Notations:

$\vec{X}_1(t)$, $\vec{X}_2(t)$: 2D position of bacteria 1 and 2 at time x_1, vector
$\vec{X}_3(t)$: relative position of x_1 and x_2, vector
$L(t)$: relative distance between two bacteria, scalar
$\vec{V}(t)$: relative true speed
$\dot{L}(t)$: change rate of $L(t)$ = projection of $\vec{V}(t)$for cell-cell axis

Theoretical Model

1. Introduction and general aims

In this section, we present our particle-based model of *Neisseria meningitidis* aggregates. The aim is to show how the intermittent active attraction between bacteria mediated by T4P controls the physical properties of aggregates, and in particular yields fluidization. The analysis presented below is twofold. We first present numerical simulations of the model, which are based on experimentally measured parameters; this part reproduces quantitatively the experimental results and thus validates the model, which highlights the role of the intermittent dynamics of T4P. Second, we present an approximate mean-field treatment, based on simplifying

assumptions, which aims at providing analytical arguments to support our findings that (i) the phase diagram is critically controlled by t_{ON}/t_{OFF} and (ii) the single particle diffusion in the liquid phase can be higher than in the dispersed phase (fluidization).

We start by defining the model in a general and minimal way. Each bacterium is modeled as an apolar spherical solid particle of radius r_0. Particles are labeled by index $i \in [1,\ N]$; their positions are denoted by $\mathbf{x}_i$. Because of thermal fluctuations of the fluid environment, each particle, if isolated, diffuses with a diffusion coefficient given by the Stokes – Einstein law, $D = k_B T/\gamma$, where γ is the viscous friction. In addition, each particle i may experience a pairwise interaction force induced by particle j that we decompose into a repulsive part $\mathbf{F}^r_{ij}$, modeling hard core repulsion between particles, and a stochastic short-range attractive force $\epsilon_{if}\mathbf{F}^p_{ij}$ mediated by pili; $\mathbf{F}^r_{ij} = -\mathbf{F}^r_{ji}$ and $\mathbf{F}^p_{ij} = -\mathbf{F}^p_{ji}$ is imposed by Newton's third law. Here the random variable $\epsilon_{if} = \epsilon_{ji}$ is set to 1 if pili of particle i and j are bundled and transmit forces ("on" state), and else to 0 ("off" state). In what follows, and in agreement with experiments on isolated pairs of bacteria, we will assume that all ϵ_{if} are independent and follow a classical 2-state random telegraph dynamics (Van Kampen, 2007) with constant switching rates $1/t_{ON}$ (from "on" to "off" state) and $1/t_{OFF}$ (from "off" to "on" state); we denote $p(\epsilon_{ij} = X)$ the corresponding probability that the pair $i,\ j$ is in state X. The short range of the pili force is taken into account by the cut-off distance $\left|\mathbf{x}_i - \mathbf{x}_j\right| = l_p$, beyond which $\mathbf{F}^p_{ij}$ is set to 0. The dynamics of the system can then be written as a set of Langevin equations:

$$\frac{d\mathbf{x}_i}{dt} = \frac{1}{\gamma}\left(\sum_j \mathbf{F}^r_{ij} + \epsilon_{ij}\mathbf{F}^p_{ij}\right) + \sqrt{2D}\boldsymbol{\xi}_i, \tag{1}$$

where for each pair i, j:

$$\frac{d}{dt}p(\epsilon_{ij}=1) = -\frac{1}{t_{ON}}p(\epsilon_{ij}=1) + \frac{1}{t_{OFF}}p(\epsilon_{ij}=0) \tag{2}$$

and

$$\frac{d}{dt}p(\epsilon_{ij}=0) = +\frac{1}{t_{ON}}p(\epsilon_{ij}=1) - \frac{1}{t_{OFF}}p(\epsilon_{ij}=0). \tag{3}$$

Here $\boldsymbol{\xi}_i$ is a d-dimensional Gaussian white noise with normalized components. As defined here, the model is general and describes generically any system of interacting diffusing particles with intermittent interactions. We stress that the intermittent dynamics of ε_{ij} is the key feature driving the system out of equilibrium and making it active (Marchetti et al., 2013). In the particular limit $t_{ON} \to \infty$ we recover a classical model of overdamped interacting particles at thermal equilibrium (Löwen, 1994; Barrat and Hansen, 2003).

2. Numerical simulations

Explicit choices of parameters and functional forms of $\mathbf{F}^r_{ij}$ and $\mathbf{F}^p_{ij}$ must be made to perform numerical simulations. These choices were dictated by the results of experiments involving isolated pairs of bacteria. This is recapitulated in this section.

A. Forces. We introduce the inter-particle distance $r_{ij} = \left|\mathbf{x}_i - \mathbf{x}_j\right|$ and unit vector $\mathbf{e}_{ij} = (\mathbf{x}_j - \mathbf{x}_i)/r_{ij}$. The sum in the right-hand side of Equation (1) involves all particles within distance $l_p (r_{ij} < l_p)$, but is further restricted to those particles j that are Voronoi neighbors of i. This mechanism avoids all spurious "crowding" effects for which particle i would have an unrealistic number of connections. Similarly, the dynamics of ε_{ij} was integrated only for Voronoi pairs $i,\ j$ such that $r_{ij} < l_p$. For numerical convenience, the repulsive force was chosen as:

$$\mathbf{F}^r_{ij} = -\frac{h}{r_{ij}} \times \theta(2r_0 - r_{ij})\mathbf{e}_{ij}, \tag{4}$$

with h arbitrarily large (see the following paragraph for explicit value) to ensure that $r_{ij} \geq 2r_0$. Here $\theta(x)$ denotes the step function, defined by $\theta(x<0)=0$ and $\theta(x>0) = 1$. The attractive force $\mathbf{F}^p_{ij}$ accounts for active processes inducing the retraction of pili; it is observed experimentally that retraction occurs at an approximately constant speed v_r up to a maximal force magnitude F_m. In order to reproduce these observations, we introduced:

$$\Phi^p_{ij} = \frac{\gamma}{2}\frac{\left(r_{ij} - \left(r^0_{ij} - v_r(t_{ij} + \delta t)\right)\right)}{\delta t}\mathbf{e}_{ij}, \tag{5}$$

where δt is the time step used in simulations. Here t_{ij} is the time spent since the creation of the link ij. By defining $\mathbf{F}^p_{ij} = \Phi^p_{ij}$ if $\left|\Phi^p_{ij}\right| < F_m$, and $\mathbf{F}^p_{ij} = F_m\mathbf{e}_{ij}$ if $\left|\Phi^p_{ij}\right| \geq F_m$, we reproduced the observed behavior of attraction at constant speed up to a maximal force.

B. Parameters and Initial Conditions. Equations (1), (2), and (3) where then integrated numerically in C++ using the Euler-Maruyama integration scheme for the choice of parameters, obtained thanks to experiments on isolated pairs of bacteria, summarized in the following:

Noise amplitude: $\mathbf{4D}$ = 1.03 $\mu m^2/s$ (Experiments)
Friction coefficient: $\gamma = \mathbf{6\pi\eta r_0}$ = 1.8 × 10^{-8} kgs^{-1} (Stokes-Einstein)
Max. repulsion force: $\boldsymbol{h}$ = 45 pN (Adjustable)

Max. pili force: F_m = 9 pN (Experiments)
Particle diameter: $d_0 = 2r_0$ = 1 μm (Experiments)
Pilus length: l_p = 6 μm (Experiments)
Initial box size: r_{max} = 40 μm (Adjustable)
Number of particles: $N = 10^3$-10^4 μm (Adjustable)
Time step: $\delta t = 10^{-5}$-10^{-6} s (Adjustable)
Transition time OFF → ON: t_{OFF} = 15 s or varying (Experiments)
Transition time ON → OFF: t_{ON} = 15 s or varying (Experiments)

The dynamics was implemented in a two-dimensional unbounded space, and the initial state was drawn randomly (excluding overlaps between particles) with particles in a square box of size $r_{max} \times r_{max}$ (typically $r_{max} = 40\mu m$).

C. Phase diagram. Numerical simulations revealed a very good agreement with experimental observations as explained in the main text; in addition, they showed very different behaviors upon varying t_{OFF}, which was chosen as a control parameter. In particular, we identified solid, liquid and gas phases (Figure 4B). It should be noted that we focused on the dependence on t_{OFF}, which is the main new feature of the model, and left the analysis of the dependence on particle density, which would require a different numerical set-up, for further work. Since numerical simulations were performed in unbounded space, the phase diagram of Figure 4B is not a standard representation with fixed particle density or pressure, even if it is expected to be qualitatively close.

Solid-Liquid. The solid-liquid transition is determined numerically using the MSD (mean squared displacement) of particles defined by:

$$\mathrm{MSD}(t) = \frac{1}{N}\sum_{i=1}^{N}\frac{1}{T-t}\int_0^{T-t} d\tau |\mathbf{x}_i(t+\tau) - \mathbf{x}_i(\tau)|^2, \tag{6}$$

which is an average over both time and particles. The liquid phase is then characterized by a linear growth of the MSD with time, with however different regimes that reflect the various timescales of the problem. We focused on relatively short times scales (typically $\lesssim$ 10 s), which is the relevant timescale of experimental data, and the diffusion coefficient D was deduced by fitting the MSD data to $\mathrm{MSD}_s(t) = 4Dt$ at these timescales. At this timescale interactions between particles are probed, but larger scale heterogeneities and finite size of aggregates are negligible. The solid phase was characterized by a short time diffusive regime saturating to a plateau. In fact, in the solid phase, the behavior of the MSD is more typical of sub-diffusion due to caging effects than of normal diffusion; we nevertheless proceeded with the fit, which then yielded essentially vanishing D values. The transition was then characterized by the sharp increase of D from near-zero in the solid phase to finite values in the liquid phase (Figure S3E).

2. Liquid-Gas. The liquid-gas transition was determined numerically by analyzing the expansion in unbounded space of the initial aggregate, measured by its radius of gyration:

$$R_{gyr}(t) = \sqrt{\frac{1}{N}\sum_i |\mathbf{x}_i(t) - \langle \mathbf{x}_i(t)\rangle_i|^2}, \tag{7}$$

where $\langle x_i(t)\rangle_i$ is the location of the center of mass of all particles at time t. In the liquid phase the initial droplet is stable (even though it equilibrates with its vapor, and rounds up from its initial square shape), so that $R_{gyr}(t)$ is practically constant in time. In the gas phase a free diffusive expansion is obtained, and $R_{gyr}(t)$ is expected at long times to behave as $R^2_{gyr}(t) \sim 4Dt$. We therefore computed numerically the expansion rate (dR^2_{gyr}/dt), which sharply increased from near zero values to finite values at the liquid gas transition (Figures S3F and S3G).

3. Local diffusion coefficient

In order to define a local diffusion coefficient inside aggregates, we indexed particles according to their initial distance $r_i(t_0) = |\mathbf{x}_i(t_0) - \langle \mathbf{x}_i(t_0)\rangle_i|$ from the center of the aggregate (the initial time t_0 was chosen after the rounding up of the initially-square aggregate.) The MSD was then computed according to Equation (6) for all particles in concentric layers of width 1μm centered on $\langle \mathbf{x}_i(t_0)\rangle$ (Figures S3H and S3I), and the diffusion coefficient D_i was deduced from a linear fit. Note again that the core of the aggregate being quasi-solid, the behavior there may not be strictly diffusive, but could be sub-diffusive. This analysis revealed an increase of the diffusion coefficient with the distance from the center of the aggregate, and showed that the diffusion coefficient can reach values that are higher than in the gas phase (high diffusion or fluidized phase), as discussed in the main text.

3. Mean field analysis

To conclude this section, we provide simple scaling arguments to interpret the above results. We start from the minimal formulation of section I, and further assume that both forces $\mathbf{F}^r_{ij}$ and $\mathbf{F}^p_{ij}$ derive from a potential: $\mathbf{F}^r_{ij} = -\nabla_i V^r(r_{ij})$ and $\mathbf{F}^p_{ij} = -\nabla_i V^p(r_{ij})$. In the "on" state, the resulting potential $V^O(r_{ij}) = V^r(r_{ij}) + V^p(r_{ij})$ is characterized by a typical depth E^O of the bound state and a finite range of the order of l_p. Note that this hypothesis, while it allows for a mapping to a classical physical problem, misses the properties of pili retraction that are taken into account in the numerical simulation above. A quantitative agreement with experiments is therefore not expected in the analysis below.

A. Phase Diagram. A mean field analysis can be proposed by assuming that $t_{ON}, t_{OFF} \ll t_D = l_p^2/D$. While this hypothesis is reasonable for the WT, it is not satisfied for all mutants. Equation (1) can then be averaged over an intermediate timescale τ such that $t_{ON}, t_{OFF} \ll \tau \ll t_D$ (adiabatic elimination), which yields:

$$\frac{d\mathbf{x}_i}{dt} = -\frac{1}{\gamma}\left(\sum_j \nabla_i V^e(r_{ij})\right) + \sqrt{2D^e}\boldsymbol{\xi}_i, \tag{8}$$

with the effective potential:

$$V^e(r_{ij}) = V^r(r_{ij}) + \frac{t_{ON}}{t_{ON}+t_{OFF}} V^p(r_{ij}), \tag{9}$$

which can be written $V^e = \frac{t_{ON}}{t_{ON}+t_{OFF}} V^O$ for hard-core repulsion potentials. Note that here we also assume that $t_{ON}, t_{OFF} \ll \gamma l_p^2/E^O$. Here D^e accounts for both thermal fluctuations and fluctuations of the pili force, which will be discussed below. The problem is then mapped to a classical problem of interacting particles at thermal equilibrium. This class of problem has been studied extensively in the physics literature (Löwen, 1994; Barrat and Hansen, 2003), and a classical argument shows that liquid-gas and solid-liquid transitions are then observed at critical levels of noise such that:

$$\frac{\gamma D^e_{lg}}{E^e} = \theta_{lg} \text{ and } \frac{\gamma D^e_{sl}}{E^e} = \theta_{sl}, \tag{10}$$

where E^e is the energy scale of V^e and θ_{lg}, θ_{sl} are dimensionless values independent of t_{ON}, t_{OFF} which depend on the particle density and specific shape of V^O. For hard-core repulsion one has $E^e = \frac{t_{ON}}{t_{ON}+t_{OFF}} E^O$, so that the following conditions hold at the liquid-gas and solid-liquid transitions:

$$\frac{\gamma D^e_{lg}}{\theta_{lg} E^O} = \frac{t_{ON}}{t_{ON}+t_{OFF}}(liquid - gas) \text{ and } \frac{\gamma D^e_{sl}}{\theta_{sl} E^O} = \frac{t_{ON}}{t_{ON}+t_{OFF}}(solid - liquid). \tag{11}$$

Importantly, this analysis shows that both liquid-gas and solid-liquid transitions can be predicted from the analysis of a classical problem of equilibrium fluid. In the limit $t_{ON}, t_{OFF} \to 0$, a scaling analysis suggests D^e depends on t_{ON}, t_{OFF} only through the ratio t_{ON}/t_{OFF}. This analysis therefore suggests that both transitions depend on t_{ON}, t_{OFF} only through the ratio t_{ON}/t_{OFF}, which means that both transitions are characterized by a linear relationship between t_{ON} and t_{OFF}, as experimentally observed. This simple scaling analysis is based on the assumption that $t_{ON}, t_{OFF} \to 0$, meaning that t_{ON}, t_{OFF} are negligible compared to the other timescales l_p^2/D and $\gamma l_p^2/E^O$ of the problem. Note that this is not necessarily valid in all regimes experimentally studied. It however yields the correct dependence on t_{ON}, t_{OFF} and provides a physical interpretation of the observed phase diagram of this active fluid model.

B. Fluidization. Last, we discuss the mechanism responsible for fluidization in the liquid phase, which requires to refine the above mean field treatment. The main ingredient is that the intermittent dynamics of ε_{ij} induces a fluctuating contribution of the pili force that we denote by $\mathbf{f}_a$, which enters the noise term of amplitude D^e. This active noise $\mathbf{f}_a$ adds to the thermal noise $\mathbf{f}_T = \sqrt{2D}\boldsymbol{\xi}$. In a first approximation, we neglect the correlations of the active noise and write it as a Gaussian white noise; this assumption is valid in the limit $t_{ON}, t_{OFF} \to 0$.

The active noise can then be written $\mathbf{f}_a = \sqrt{2D_a}\boldsymbol{\xi}'$, where ξ' is a normalized d-dimensional Gaussian white noise. The determination of the active diffusion coefficient requires further physics work and is here only estimated as:

$$D_a \propto \left(\frac{E^O}{\gamma l_p}\right)^2 \frac{t_{ON}^2}{t_{ON}+t_{OFF}}. \tag{12}$$

Finally, the dynamics can be rewritten as:

$$\frac{d\mathbf{x}_i}{dt} = -\frac{t_{ON}}{\gamma(t_{ON}+t_{OFF})}\left(\sum_j \nabla_i V^O(r_{ij})\right) + \sqrt{2(D+D_a)}\boldsymbol{\xi}_i, \tag{13}$$

with $D^e = D + D_a$. Hence, the problem can be mapped again to a classical problem of interacting particles at thermal equilibrium (Löwen, 1994; Barrat and Hansen, 2003), with however an effective temperature:

$$T_e = \frac{\gamma D^e}{k_B} = \frac{\gamma(D+D_a)}{k_B} = T + T_a. \tag{14}$$

Qualitatively, this shows that the intermittent dynamics of the pili force induces a higher diffusion coefficient: the system thus behaves as an anomalously fluidized liquid, as discussed in the main text. A scaling analysis of the problem then shows that the diffusion coefficient D_s^a of a particle in the liquid phase (self-diffusion) satisfies:

$$D_s^a = D_s\left(\frac{t_{ON}}{t_{ON}+t_{OFF}}V^O, T_e\right) = \frac{t_{ON}}{t_{ON}+t_{OFF}}D_s\left(V^O, T_e\frac{t_{ON}+t_{OFF}}{t_{ON}}\right), \tag{15}$$

where $D_s(V,T)$ is the classical diffusion coefficient of a particle in fluid with interaction potential V at equilibrium at temperature T. The diffusion coefficient in the active liquid is thus fully determined by the knowledge of the diffusion coefficient of a classical liquid, taken with an interaction potential V^O and a temperature $T_e(t_{ON} + t_{OFF})/t_{ON}$. This problem has been studied at length in the physics literature (Löwen, 1994; Barrat and Hansen, 2003), and in general cannot be solved analytically. It is however useful to analyze its behavior close to the liquid-gas transition, where one has $D_s \sim k_B(T/\gamma_e)$, where $\gamma_e > \gamma$ is an effective friction. This yields:

$$D_s^a \sim \frac{k_B T}{\gamma_e} + \frac{k_B T_a}{\gamma_e}. \tag{16}$$

This shows that the active contribution $k_B(T_a/\gamma_e)$ if T_a is large enough, can yield values that are larger than the diffusion coefficient $k_B(T_a/\gamma_e)$ in the gas phase. This explains the observed fluidization effect that we observe.

Micro-channels fabrication

Micro-channels were a kind gift from Matthieu Piel's lab, and were prepared as previously described (Heuzé et al., 2011). Briefly, a 10:1 mixture of PDMS Sylgard 184 or RTV614 silicone elastomer and curing agent was poured onto the epoxy replica and cured at 65°C for 3h, to prepare micro-channels of different sizes (12 μm X 8 μm, 5 μm X 4 μm).

Micro-channels experiments and quantification

Channel inlets were punched with a 2.5-mm puncher before bonding. The PDMS chamber and an Ibidi μ-slide 2 well with glass-bottom dish (80287, Biovalley) were exposed to 45 s oxygen plasma for bonding. The binding was left to strengthen in a 65°C oven for 1 h. Finally, chambers were exposed for 10 min to UV light for sterilization (UVO cleaner, Jelight), and incubated with RPMI + 10% FBS for at least 1 h at 37°C and 5% CO_2 before cell loading. Bacteria from 2 hs pre-cultures in the same medium were re-suspended at a final OD 0.1, vortexed and then injected in the chamber. Finally, the chamber was immersed in medium to prevent evaporation. Bright-Field and fluorescence time-lapses of iRFP-expressing WT and *pilT* strains were acquired in parallel in two separated wells (Ibidi) over 10 hs were acquired at 37°C 5% CO_2 on an inverted spinning-disk confocal microscope (Ti-eclypse, Nikon) with 20 x magnification. Images were acquired with a EMCCD camera (Evolve, Photometrics) using Metamorph Imaging Software (Molecular Devices). Image processing and analysis of the temporal evolution of aggregate size were performed using Fiji software (Schindelin et al., 2012).

Spinning disk intravital microscopy

SCID/Beige mice grafted with human skin were anaesthetized by spontaneous inhalation of isoflurane in oxygen and maintained at 37°C with a heating pad. The tail vein was cannulated to administer fluorescent dyes and bacteria. Surgery of the human skin for intravital imaging was performed as previously described (Ho et al., 2000). Briefly, a midline incision was made from the neck to the lower back and the skin supporting the human skin graft was flipped and secure onto an aluminum custom made heated pedestal (36°C). The human microvasculature within the graft was exposed by carefully removing the excess of connective tissue. The skin flap was covered with a coverslip sealed with vacuum grease and continuously moistened with warmed saline buffer (36°C) during the observations. Tissue was allowed to stabilize for 30 minutes before data acquisition.

Intravital microscopy of the human skin microvascular network was performed using a Leica DM6 FS upright microscope equipped with a motorized stage. The microscope is fitted with HC Fluotar 25 x/0.95 objective lens (Leica) and is mounted on an optical table to minimize vibration. The microscope is coupled to a Yokogawa CSU-W1 confocal head modified with Borealis technology (Andor). To visualize human vessels, 50 μg of UEA-1 lectin (VectorLabs) conjugated with AF750 was intravenously injected 30 minutes prior to imaging. 4 to 6 fields of view containing human vessels were selected per mice and N = 3 mice per bacteria strain (WT and *pilT*) were infected by intravenous injection of 100 μl of 10^8 CFU/ml iRFP-expressing bacterial culture (10^7 CFU total). Z stacks of *xy* planes (z-step = 2 μm) were acquired every 10 minutes during 3 hours with 637 and 730 nm laser excitation wavelengths to image human vessels and bacteria. Fluorescence detection was made by a sCMOS 2048 × 2048 pixel camera (Orca Flash v2+, Hamamatsu) with 2x2 binning. Metamorph software (Molecular Devices) was used to drive the confocal microscope and acquisition. Images were post-processed (deconvolution and photobleaching correction) using Huygens software (Scientific Volume Imaging) and edited on Fiji (Schindelin et al., 2012).

QUANTIFICATION AND STATISTICAL ANALYSIS

Number of replicates and number of animals/cells/aggregates analyzed per replicate are specified in corresponding legends. All experiments were replicated at least 3 times, and statistical comparisons were carried out using GraphPad Prism with two-tailed Student's t tests. Differences were considered to be significant when p values were below 0.05. Details on sample numbers and significance levels are given in figure legends. In all figures, measurements are reported as mean ± standard deviations (s.d.).

DATA AND SOFTWARE AVAILABILITY

MATLAB custom software for post-processing bacterial tracks and simulations script will be provided upon request to the Lead Contact (guillaume.dumenil@pasteur.fr).

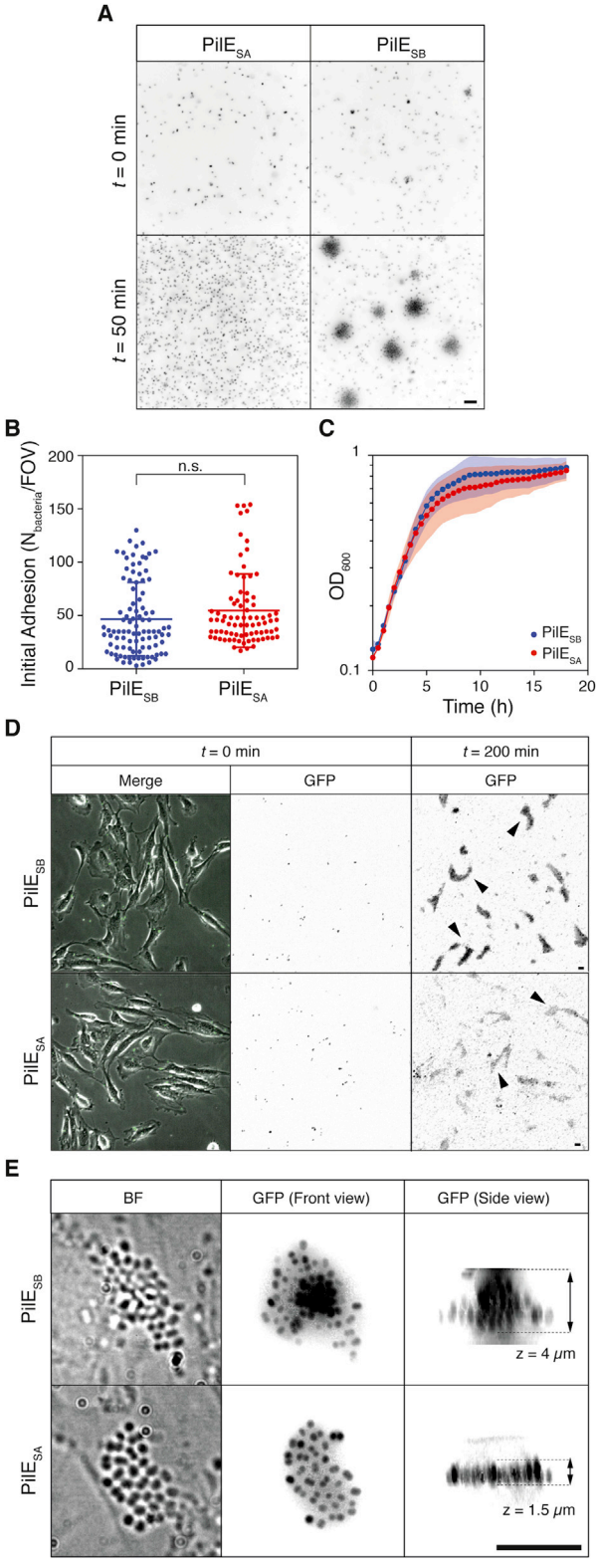

Figure S1. *In Vitro* Characterization of the Pilin Variants $PilE_{SA}$ and $PilE_{SB}$, Related to Figure 1

(A) Representative pictures of the GFP-expressing pilin variants $PilE_{SB}$ and $PilE_{SA}$ (OD_{600} = 0.3) at time *t* = 0 and 50 min after vortexing. Images are representative of n = 3 independent experiments. Scale bar, 10 μm.

(legend continued on next page)

(B) Initial adhesion of the GFP-expressing pilin variants $PilE_{SB}$ (indicated in blue) and $PilE_{SA}$ (indicated in red) on HUVECs in the presence of a shear stress of 0.044 dynes/cm^2. Images were acquired 10 min post flow application and adherent bacteria were counted over multiple fields of view. Corresponding mean values and standard deviations are indicated for each condition. Images are representative of n = 5 independent experiments, N = 20 fields of view/bacterial strain for each experiment. P value = 0.1224.

(C) Growth curves of the pilin variants $PilE_{SB}$ (indicated in blue) and $PilE_{SA}$ (indicated in red) over 18 h, expressed as absorbance values at λ = 600 nm (OD_{600}). Dots and colored areas indicate average values and standard deviations respectively. n = 3 independent experiments.

(D) Representative phase contrast and fluorescence pictures of the GFP-expressing pilin variants $PilE_{SB}$ and $PilE_{SA}$ adhering on HUVECs at time t = 0 and 200 min. Black arrows point at typical colonies formed by the two strains upon bacteria proliferation. Note that the aggregative $PilE_{SB}$ variant lead to much denser microcolonies compared to the non-aggregative $PilE_{SA}$ variant. Images are representative of n = 3 independent experiments. Scale bar, 10 μm.

(E) Representative high-resolution bright field and fluorescence 3D reconstructions of bacterial colonies formed by the GFP-expressing pilin variants $PilE_{SB}$ and $PilE_{SA}$ on HUVECs at time t = 200 min, with corresponding front and side views. Note that the aggregative $PilE_{SB}$ variant lead to 3D microcolonies with multiple bacteria layers while the non-aggregative $PilE_{SA}$ variant form 2D microcolonies of a single bacteria layer. Images are representative of n = 3 independent experiments. Scale bar, 10 μm.

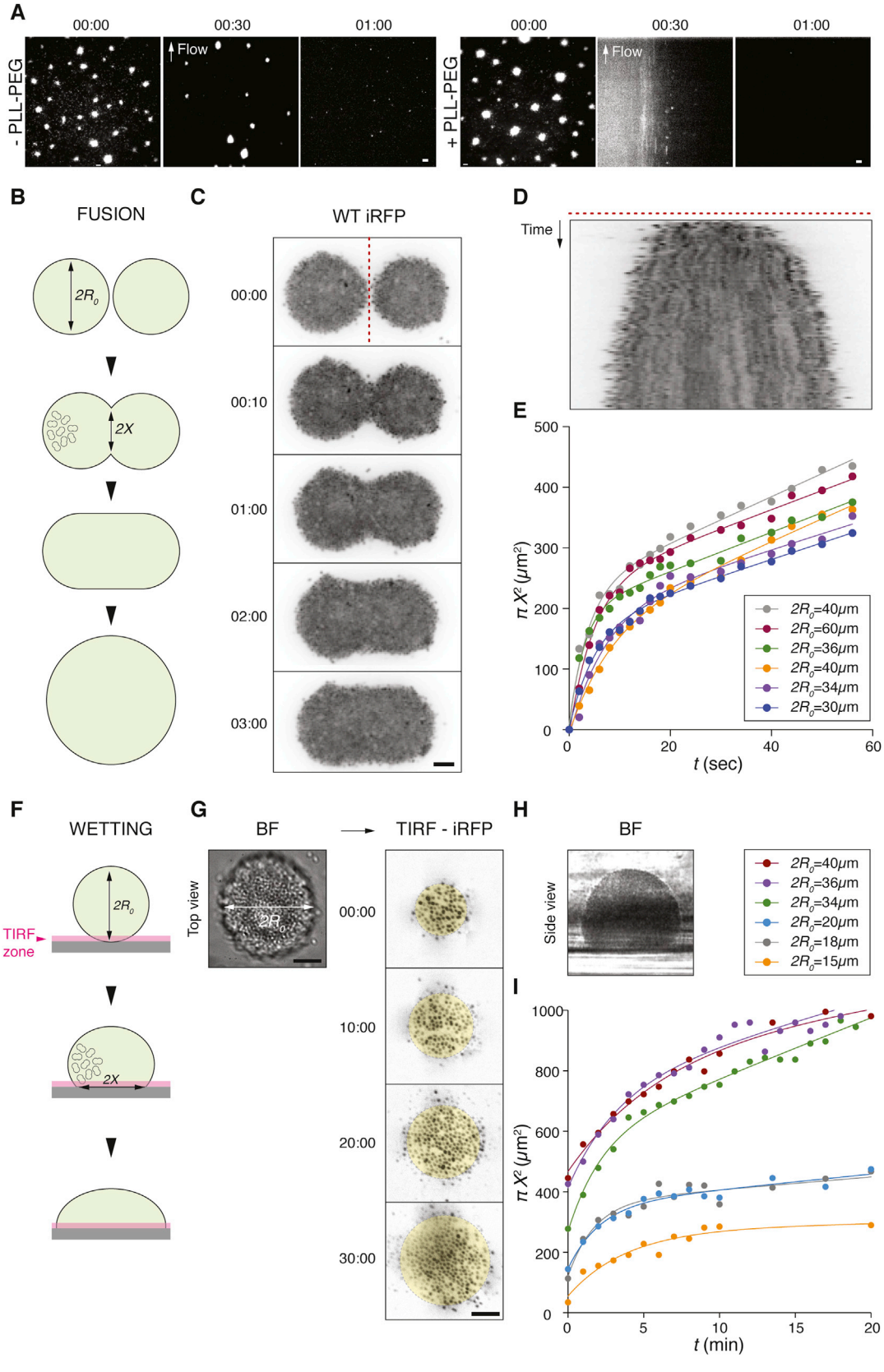

(legend on next page)

Figure S2. *In Vitro* Characterization of *N. meningitidis* WT Aggregates, Related to Figure 2

(A) On the left, WT iRFP aggregates formed inside a plastic bottom channel (Ibidi) were submitted to low intensity flow for 1 min. On the right, aggregates formed on PLL-PEG treated plastic bottom were submitted to the same flow. Note that in the case of a PLL-PEG treated substrate aggregates are immediately carried away by the flow, while on simple plastic they resist for a short time, showing weak adhesion. Time is indicated in min:sec. Images are representative of n = 3 independent experiments. Scale bar, 10μm.

(B) Schematic of fusion between two liquid droplets with the same initial radius, R_0. Droplets get in contact and the contact area with radius X rapidly increases to finally equilibrate at a final value corresponding to a spherical droplet of doubled volume.

(C) Time lapse of fusion between two iRFP-expressing bacterial aggregates. A red dotted line indicates the contact region between aggregates which is used to generate kymographs. Time is indicated in min:s. Images are representative of n = 3 independent experiments. Scale bar, 10 μm.

(D) Corresponding kymograph of the fusion event shown in (B).

(E) Temporal evolution of the contact area between two fusing aggregates for various aggregate pairs of different initial size (indicated in the legend by $2R_0$). n = 3 independent experiments, N = 6 aggregate pairs.

(F) Schematic of wetting of a liquid droplet of initial radius R_0 on an adhesive substrate. The aggregate gets in contact with the substrate and progressively spread by increasing its contact area to finally equilibrate at a final value. The TIRF region for accurately visualizing the contact area is highlighted in pink.

(G) Bright-field and then TIRF time lapse of wetting of an iRFP-expressing bacterial aggregate over a lectin-coated glass substrate. Contact area over time is highlighted in yellow. Images are representative of n = 3 independent experiments. Time is indicated in min:s. Scale bar, 10 μm.

(H) Bright field side view of a representative aggregate wetting on the lectin-coated glass substrate after 30 min.

(I) Temporal evolution of the contact area of various aggregates with different initial sizes (indicated in the legend by $2R_0$) wetting on a lectin-coated glass substrate. n = 3 independent experiments, N = 6 aggregate pairs.

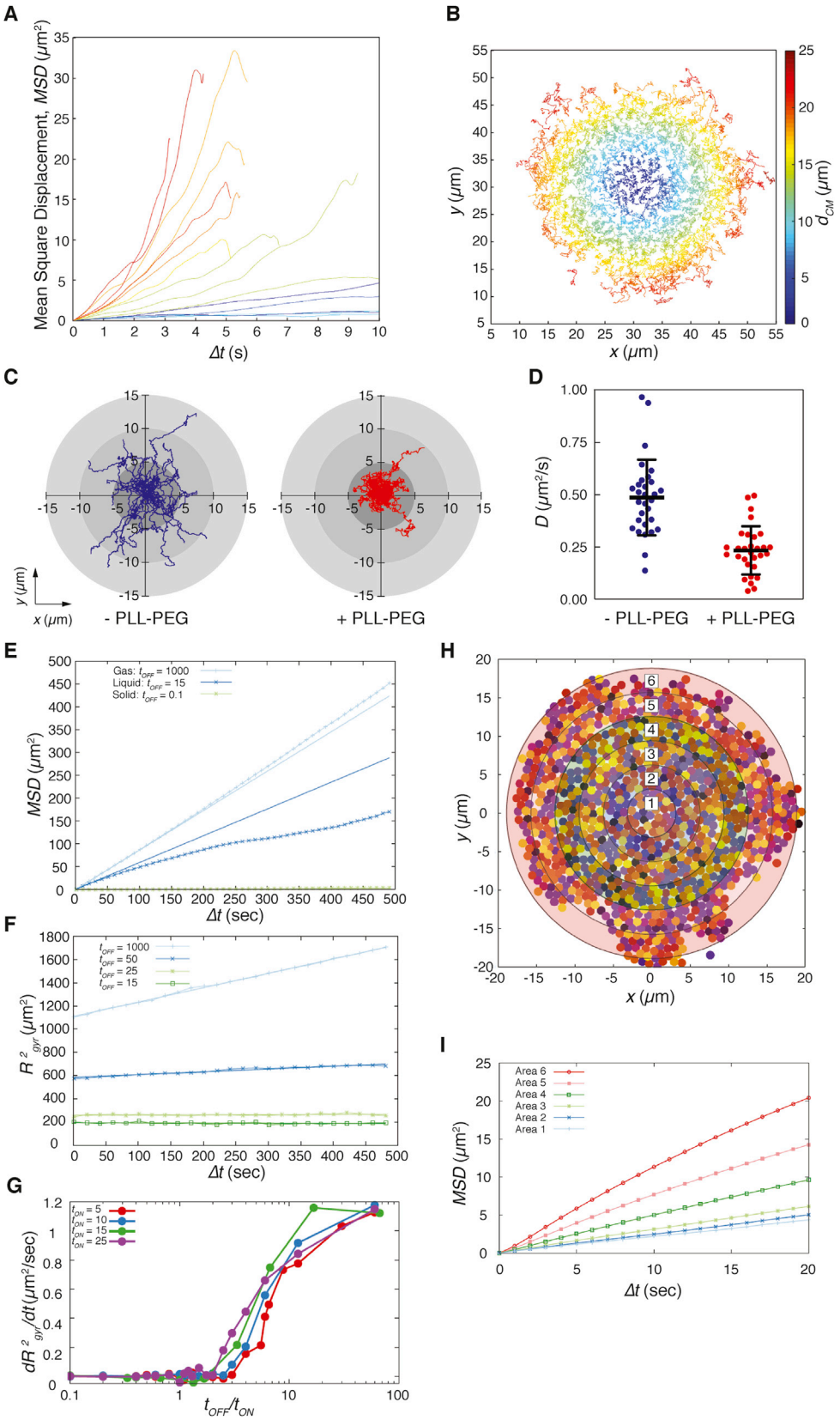

(legend on next page)

Figure S3. *In Vitro* and *In Silico* Quantification of Single Bacterial Motility within Aggregates and in Isolation, Related to Figures 3–6

(A) Mean square displacement of individual bacteria inside an aggregate. Curve color code depends on the distance to the center, as in Figure S1B. Analysis is representative of n = 3 independent experiments.

(B) Color coded bacterial tracks within a single aggregate over 20 s. Analysis is representative of n = 3 independent experiments.

(C) Trajectories of individual bacteria moving on a plastic substrate over 10 s. On the left, bacteria twitch and move directionally on non-treated plastic (blue tracks); on the right, bacteria show diffusive movement on PLL-PEG treated plastic (red tracks). n = 3 independent experiments, N = 30 tracks/bacterial strain.

(D) Corresponding diffusion coefficients of individual bacteria on the two substrates (Blue: without PLL-PEG; Red: with PLL-PEG). n = 3 independent experiments, N = 30 tracks/bacterial strain.

(E) Typical Mean Square Displacement obtained in numerical simulations in gas, liquid, and solid phases. Numerical simulations (symbols) and linear fits (thick plain lines of corresponding color) are displayed. Simulations were performed with indicated parameters values (see the Method Details) for a simulation time of 1000 s. MSD was measured after a relaxation time of 500 s, so that a quasi-steady state is reached. Here an average over all particles of the aggregate is performed.

(F) Typical $R^2_{gyr}(t)$ obtained in numerical simulations in gas and liquid phases (in μm^2). Numerical simulations (symbols) and linear fits (thick plain lines of corresponding color) are displayed.

(G) Time derivative dR^2_{gyr}/dt (in $\mu m^2/s$) as a function of t_{OFF}/t_{ON}. This quantity transitions from near zero (liquid phase) to finite values (gas phase). Simulations were performed with indicated parameters values (see the Method Details) for a simulation time of 1000 s.

(H) Local MSD as a function of the particle position in the aggregate in the liquid phase ($t_{ON} = t_{OFF} = 15$ s). The aggregate is divided into 6 concentric regions labeled from inside to outside (units in μm).

(I) Local MSD as a function of the particle position in the aggregate in the liquid phase ($t_{ON} = t_{OFF} = 15$ s). Numerical simulations (symbols) were performed with indicated parameters values (see the Method Details) for a simulation time of 1000 s. MSD (in μm^2) was measured after a relaxation time of 500 s, so that a quasi-steady state is reached.